8-2014

Towards Image-Guided Pediatric Atrial Septal Defect Repair

Fuad Mefleh
Clemson University

Towards Image-Guided Pediatric Atrial Septal Defect Repair

A Dissertation
Presented to
the Graduate School of
Clemson University

In Partial Fulfillment
of the Requirements for the Degree
Doctor of Philosophy
Bioengineering

---

by
Fuad Nedal Mefleh
August 2014

Accepted by:
Dr. David Kwartowitz, Committee Chair
Dr. Delphine Dean
Dr. Dan Simionescu
Dr. G. Hamilton Baker

Abstract

Congenital heart disease occurs in 107.6 out of 10,000 live births, with Atrial Septal Defects (ASD) accounting for 10% of these conditions. Historically, ASDs were treated with open heart surgery using cardiopulmonary bypass, allowing a patch to be sewn over the defect. In 1976, King et al. demonstrated use of a transcatheter occlusion procedure, thus reducing the invasiveness of ASD repair. Localization during these catheter based procedures traditionally has relied on bi-plane fluoroscopy; more recently trans-esophageal echocardiography (TEE) and intra-cardiac echocardiography (ICE) have been used to navigate these procedures. Although there is a high success rate using the transcatheter occlusion procedure, fluoroscopy poses radiation dose risk to both patient and clinician. The impact of this dose to the patients is important as many of those undergoing this procedure are children, who have an increased risk associated with radiation exposure. Their longer life expectancy than adults provides a larger window of opportunity for expressing the damaging effects of ionizing radiation. In addition, epidemiologic studies of exposed populations have demonstrated that children are considerably more sensitive to the carcinogenic effects radiation.

Image-guided surgery (IGS) uses pre-operative and intra-operative images to guide surgery or an interventional procedure. Central to every IGS system is a software application capable of processing and displaying patient images, registration

between multiple coordinate systems, and interfacing with a tool tracking system. We have developed a novel image-guided surgery framework called Kit for Navigation by Image Focused Exploration (KNIFE). This software system serves as the core technology by which a system for reduction of radiation exposure to pediatric patients was developed. The bulk of the initial work in this research endevaour was the development of KNIFE which itself went through countless iterations before arriving at its current state as per the feature requirements established.

Secondly, since this work involved the use of captured medical images and their use in an IGS software suite, a brief analysis of the physics behind the images was conducted. Through this aspect of the work, intrinsic parameters (principal point and focal point) of the fluoroscope were quantified using a 3D grid calibration phantom. A second grid phantom was traversed through the fluoroscopic imaging volume of II and flat panel based systems at 2 cm intervals building a scatter field of the volume to demonstrate pincushion and S distortion in the images. Effects of projection distortion on the images was assessed by measuring the fiducial registration error (FRE) of each point used in two different registration techniques, where both methods utilized ordinary procrustes analysis but the second used a projection matrix built from the fluoroscopes calculated intrinsic parameters. A case study was performed to test whether the projection registration outperforms the rigid transform only.

Using the knowledge generated were able to successfully design and complete mock clinical procedures using cardiac phantom models. These mock trials at the beginning of this work used a single point to represent catheter location but this was eventually replaced with a full shape model that offered numerous advantages. At the conclusion of this work a novel protocol for conducting IG ASD procedures was developed. Future work would involve the construction of novel EM tracked tools, phantom models for other vascular diseases and finally clinical integration and use.

Dedication

I dedicate this work to my family. My parents Nedal and Jeanne who provided me with the love and resources to bring my dreams to life. Without their constant encouragement and guidance I couldn't have made it to this point. I owe my success to their sacrifices and for that I am enternally grateful. My younger brother Hashim who inspires me each day to become even better than I am today and my youngest brother Ahmed who reminds me to be compassionate and kind. My fiance Maliha who stood by me through the good and bad times, I wish for us a lifetime of eternal happiness. Lastly, my uncle Yousef who kept me fed with his always amazing home cooked food. This work is not only the culmination of the sacrifices I have made but also of all of yours.

Acknowledgments

It goes without saying that my friend, mentor and advisor Dr. David Kwartowitz played a large part in me reaching this point and I would like to extend my utmost thanks and gratitude for the role he played. From the long talks in the car on the way to Charleston, encouragment and the fun we had with all sorts of power tools in the lab our friendship is something I will carry foward with me. Thank you Dr. Hamilton Baker for serving as the clinician on my committee and for giving your time to help develop the ideas embodied in this work. Your valuable clinical perspective and insight helped to mold this work into something that arguably has clinical value. I would like to thank Dr. Delphine Dean who is not only my committee member but was my undergraduate advisor. Her assitance through this process is appreciated and having the oppurtunity to serve as teaching assistant for her class offered me valuable experience for the next step in my carreer. I would also like to thank my final committee member Dr. Dan Simionescu. I would like to thank Dr. Anup Pillai for his advice and assitance over the past year. Finally I want to thank my best friend and lab mate Vipul Raikar for not only his assistance on this work but for his kindness and loyalty.

Table of Contents

Title Page . . . . . **i**

Abstract . . . . . **ii**

Dedication . . . . . **iv**

Acknowledgments . . . . . **v**

List of Tables . . . . . **viii**

List of Figures . . . . . **ix**

1 Introduction and Motivation **1**
1.1 Atrial Septal Defects 2
1.2 Image-Guided Surgery (IGS) 5
1.3 Radiation Risk 7

2 Development of a Novel Image-Guided Surgery System with an Open Framework **11**
2.1 Introduction 11
2.2 Methods 15
2.3 Discussion and Conclusions 26

3 Assessment of Accuracy and Distortion in Fluoroscopy for use in Image-guided Surgery **28**
3.1 Abstract 28
3.2 Introduction 29
3.3 Materials and Methods 34
3.4 Results and Discussion 40
3.5 Conclusion 48

4 Efficacy of a Novel IGS System in Atrial Septal Defect Repair . . **49**
4.1 Abstract 49
4.2 Introduction 50

4.3 Methods 53
4.4 Results 56
4.5 Discussion and Conclusions 56

5 Heuristic Estimation of Electromagnetically Tracked Catheter Shape for Image-Guided Vascular Procedures 60
5.1 Abstract 60
5.2 Introduction 61
5.3 Methods 64
5.4 Results 67
5.5 Discussion and Conclusions 68

6 Image-Guided Vascular Procedures: a feasability study 72
6.1 Introduction 72
6.2 Methods 75
6.3 Results 80
6.4 Discussion 82
6.5 Conclusion 84

7 Conclusions and Future Work 85

Bibliography 88

List of Tables

3.1 Calculated intrinsic parameters for the lateral and AP plane of the flat panel and image intensifier fluoroscope. 41

3.2 RMS error for registration between world, camera, and image point clouds in millimeters for each direction and total directional error. WC is world to camera and WI is world to image. 42

3.3 Average directional error values in millimeters for a single frame of the 2D centroid grid fluoroscope volume capture in millimeters. Error for the image intensifier fluoroscope is significantly higher than the flat panel fluoroscope. 45

3.4 RMS error values in millimeters for the registration between image points and collected tracker points as well as transformed camera points and collected tracker points. The camera coordinates produced a significantly better fit than the image points which means points should be transformed into the camera coordinate space prior to being used in a registration. 47

5.1 Hausdorff distance for each interpolation algorithm in mm for each segment of the tracked shape catheter 68

5.2 Average directional error values in millimeters for a single frame of the 2D centroid grid fluoroscope volume capture in millimeters. Error for the image intensifier fluoroscope is significantly higher than the solid state fluoroscope. 69

List of Figures

1.1 Major types of ASDs shown with atrial wall removed. Secundum ASD is the most common defect which allows blood to shunt left to right. Image copyright 2006 Patrick Lynch, reprinted under creative commons attribution license 2.5. 3
1.2 Amptatzer septal occluder, shown in a deployed state, with catheter attached. 4
1.3 AMPLATZER Septal Occluder being delivered through a sheath catheter and deployed across the defect wall before being released from the occluder wire shaft. 5

2.1 (a) Screenshot showcasing the general display of the Vanderbilt University SNARL developed image-guided surgery software ORION. (b) Medtronic's StealthStation software displaying an image-guided pedicle screw insertion procedure. The software is able to assist in planning and placement of each screw. 13
2.2 Display of DICOM metadata from a CT image data set using the open-source software MevisLab. Each tag has a name and an expected data type for use in retrieval from the stored image file. 17
2.3 Optical (a) and electromagnetic trackers (b) from Northern Digital Inc., each technology offers differing levels of accuracy, tracking volume and line of sight leading to adoption based on procedure requirements. 19
2.4 Screenshot of KNIFE load study wizard steps demonstrating how users are guided through the process of setting up a new procedure. 25
2.5 Screenshot of KNIFE displaying a bi-plane fluoroscopic image set with windows from loaded plugins surrounding it. 26

3.1 31

3.2 Overview of each step in the automated calibration technique for the lateral plane on the flat panel fluoroscope where BBs in the image are located and assigned their proper depth. (a) Original fluoroscopic image. (b) Post thresholding of fluorscopic image. (c) Connected component labels of BBs in image. (d) Centroid locations of each BB with color applied to signify different location assignments. (e) Centroid locations of each BB after depth has been assigned. Each color signifies a different depth. (f) 3D scatter plot of centroids extracted from fluoroscopic image. 37
3.3 Cardiac phantom used to assess the correction method presented. (a) Top-view. (b) Side-view. 40
3.4 Centroid grids of the 3D grid phantom where the transformed camera point cloud was registered to the world point cloud (a,c,e) and the image point cloud was registered to the world point cloud (b,d,f). . . 43
3.5 Single frame with markers connected to each neighbor to form a grid. (a) Constructed using images from the II, pincushion distortion is grossly apparent and there is slight 'S' distortion. (b) Grid from solid state detector, lines are straight and there appears to be little to no distortion. 44
3.6 Centroid grids of a single frame from the 2D grid phantom volume traversal through a flat panel and image intensifier fluoroscope. (a) The error appears to be high as many of the image points don't map well to world points which is expect for image intensifier systems due to pincushion and 'S' distortion. (b) Transformed camera points have a good fit with the world point cloud and the amount of error is significantly lower. 45
3.7 Scatter fields of the centroids from each marker as it was traversed through the imaging volume of the image intensifer 3.7a and flat panel 3.7b fluoroscopes. 46
3.8 Cardiac phantom case study images where the triangles are the transformed tracker points and the stars are the target points. (a) Image points without camera space transformation used for registration. (b) Camera space points used in calculation of registration matrix. . . . 47

4.1 CAD rendering of cardiac phantom model where transparency was used to visualize the internal defect in the chamber wall 54
4.2 (a) Fluoroscopic frame of cardiac phantom only (b) Fluoroscopic frame of cardiac phantom embedded in the chest cavity phantom where tubing simulates vasculature. 55
4.3 Average procedure times at various check points. (a) Cardiac phantom only timings, no data for fluoroscopy time at PV is available. (b) Cardiac phantom + chest cavity timings. 57

4.4 Average absorbed dose for both guidance techniques. KNIFE dosage levels are from the initial fluoroscopic cine loop collection. 58

5.1 Graphical representation of the designed EM tracked shape catheter. Tracking seeds are positioned to maximize tracking accuracy in the region of the catheter most commonly used during interventional procedures where only a small portion of the catheter is visible at any time. 65
5.2 Planar x-ray of shape catheter used for verification of seed placement along the catheter's inner lumen. 65
5.3 General workflow for segmenation and generation of catheter shape midline for a single catheter pose. (a) Original image (b, c) Threshold segmentation (d) Segmened catheter with midpoint skeleton over tracked region of catheter. 67
5.4 Full shape estimation with zoom on segment 4 of the catheter. Zoom image provided to demonstrate over estimation of shape for shape preserving and cubic spline. 68

6.1 (a) CAD design of cardiac phantom showing the separable parts. (b) Chest phantom with embedded cardiac phantom connected with polyethylene tubing to provide catheter access. 75
6.2 Mock clinical procedure setup with all equipment installed and prepared for running trials. 78
6.3 (a) KNIFE representation of catheter shape during mock procedures. (b) A fluoroscopy image of the catheter verfiying KNIFEs representaiton of catheter location and shape 79
6.4 (a) Scatter plot of radiation dose for each mock trial. It is apparent there is a high degree of variability in fluoroscopy only guided procedures and the minimum radiation used was still higher than the maximum KNIFE dose. (b) Average radiation dose comparison where it can be inferred that since it took on average of 1.26 mSv of radiation to deploy the occluder, KNIFE saves an average of 2.07 mSv for the mock trials. 81
6.5 Scatter plot of the procedure times from the mock trials showing that KNIFE was significantly slower than fluoroscopy alone. 82

Chapter 1

Introduction and Motivation

Since Wilhelm Röntgens discovery of the x-ray in 1895, the use of ionizing radiation based imaging techniques in medicine has brought immense benefits but has also led to negative side effects. While there have not been any definitive studies that show that increased use of medical radiation correlates directly cancer incidence there is qualitative evidence that this belief is valid. As children have a higher sensitivity to ionizing radiation when compared to adults, it is especially important to consider their increased risk of cancer when determining the methods used to carry out medical diagnosis and treatment. This increased sensitivity puts children that must undergo interventional cardiology procedures at even higher risk as interventional cardiology has the highest percentage (45%) of utilization of all medical ionizing radiation [10]. Reduction in the use of ionizing radiation in fluoroscopy guided vascular procedures is the primary motivation for this work and atrial septal defect repair in pediatric patients is used as an initial case study to investigate and demonstrate feasibility.

While it is the end goal of this work, a solution for every CHD diagnostic procedure and repair procedure is massive undertaking; a solution for atrial septal defect closure is provided in this dissertation as a feasibility study for future work

in the area. Many of the techniques described and presented can translate to other vascular procedures with ease and collectively they offer a standard approach for later research and development. Design and choice of the software and hardware used in the study was done in a procedure agnostic manner to maximize the benefit from work completed.

1.1 Atrial Septal Defects

Atrial septal defect (ASD) is a type of congenital heart defect characterized by a left to right shunt between the atria resulting in irregular movement of blood within the heart. At birth the inter-atrial shunt present during gestation normally closes allowing for movement of blood to the infant lungs. Atrial septal defects have a varied etiology and are classified based on anatomical location on the atrial septum. The three most prevalent types of ASDs are ostium secundum, ostium primum, and sinus venosus. Ostium secundum defects are centrally located and commonly form from the failed closing of the foramen ovale following birth, which is typically caused by the abnormal resorption of the septum primum causing incomplete adhesion to the septum secundum.

Atrial septal defects (ASD) account for 10% of congenital heart disease (CHD) with an incident rate of 1 per 1500 live births [31], or nearly 40,000 infants each year will be born with a congenital heart defect in the United States [59]. Congenital heart defects (CHD) are the most prevalent birth defect with recent trends signifying a growing rate in incidence [51]. Incidence rates of children with CHDs has driven a legislative push in South Carolina resulting in a new law requiring newborns to be screened for congenital heart diseases within 72 hours of birth [3]. While newer pulse oximetry based screening methods have increased detection rates, children born with

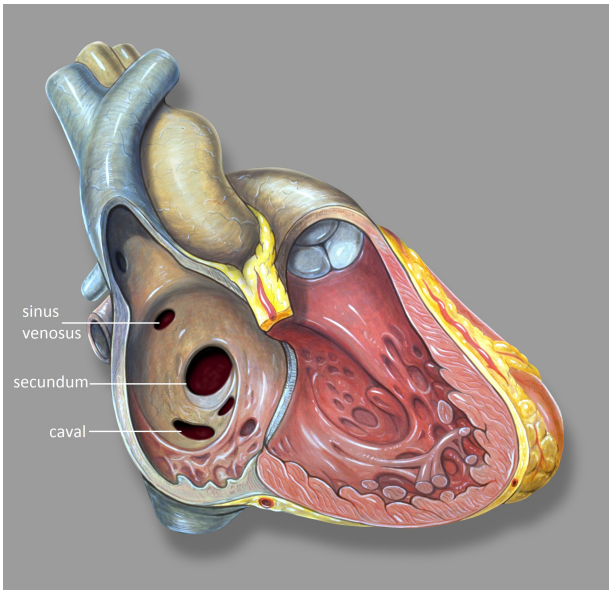

Figure 1.1: Major types of ASDs shown with atrial wall removed. Secundum ASD is the most common defect which allows blood to shunt left to right. Image copyright 2006 Patrick Lynch, reprinted under creative commons attribution license 2.5.

a CHD face multiple medical procedures and lifelong follow-up care. These medical procedures are required to abate life threatening complications but come at the risk of causing future cancers.

1.1.1 Treatment

Historically, treatment of ASD has been performed through invasive open heart surgery where either the defect is closed via suturing or by placing an occlusion patch. Each of these repair solutions involves open-heart surgery in which the patient must be placed on cardiopulmonary bypass, diverting blood from the right atria into a heart-lung machine, and back into the left atrium. In 1976, the first non-operative closure of an ASD was performed via cardiac catheterization using a mesh occluder, shaped like a double umbrella [35]. Currently a treatment option is chosen based on defect severity where milder cases involve a cardiac catheterization procedure

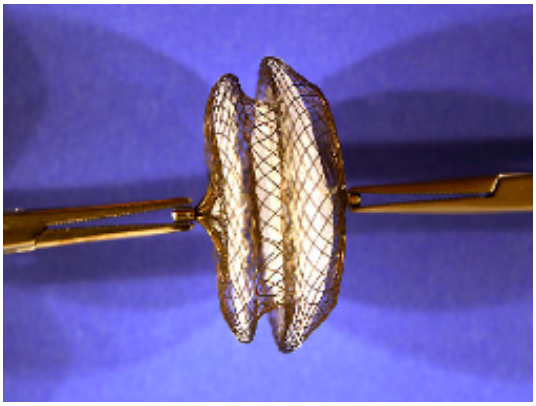

Figure 1.2: Amptatzer septal occluder, shown in a deployed state, with catheter attached.

Cardiac catheterization is used to deploy a device at a specific location to provide therapy through occlusion or patency support similar to Kings procedures. The progression of the delivery, deployment and release of a septal occluder in a patient can be seen in Figure 2. The occluder typically used in procedures and seen in the provided images is the AMPLATZER Septal Occluder (St. Jude Medical). Design of this occluder includes two variably sized discs constructed from a Nitinol wire mesh with polyester embedded for tissue ingrowth. In between the occluder discs is a narrowing forming a waist that must match the defect diameter in size. Occluder delivery is a simple medical procedure compared to open heart surgery and offers comparable closure rates following placement with lower complication rates [20].

Transcatheter closure of an ASD carries a lower risk of complication, shorter hospital stay, and shorter procedure time compared to open heart surgery [20]. As catheter interventions do not allow for direct vision of internal anatomy medical imaging is used for navigation of therapy. Typically transcatheter procedures use fluoroscopy in order to localize catheter position, which presents an increased risk of radiation exposure to the patient and to clinical staff. Traditionally bi-plane

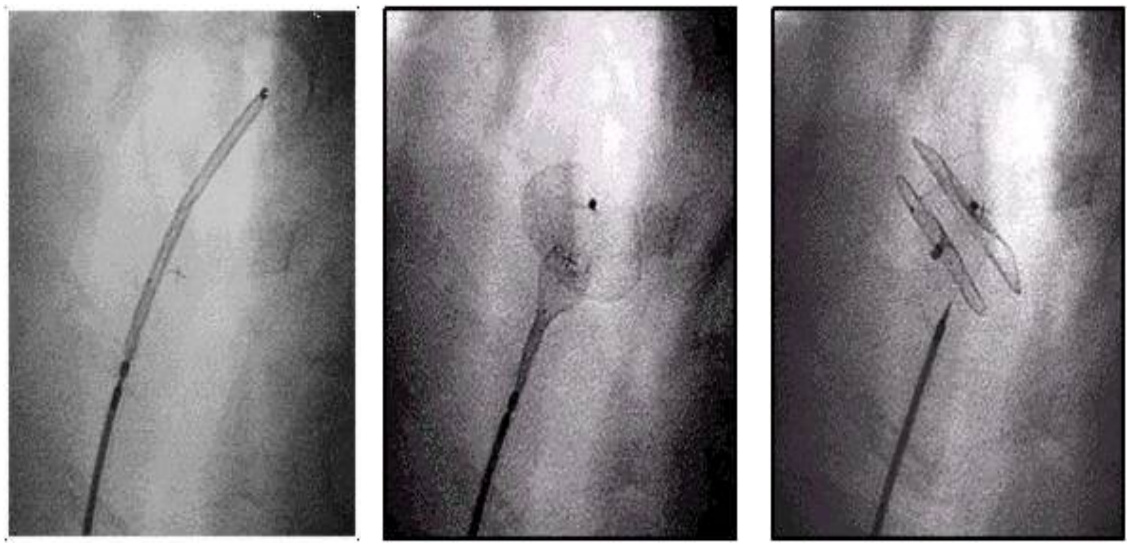

(a) Delivery (b) Deployment (c) Release

Figure 1.3: AMPLATZER Septal Occluder being delivered through a sheath catheter and deployed across the defect wall before being released from the occluder wire shaft.

fluoroscopy has been used for this navigation, as bi-plane provides visualization of all dimensions of the patient. Trans-esophageal echocardiogram (TEE) and intra-cardiac echocardiography (ICE) have been recently introduced to decrease the use of fluoroscopy. Clinical studies have also shown successful closure of ASDs using only ultrasound techniques in limited cases [62]. Transcatheter occlusion procedures offer an improvement to invasive surgery but further improvement can take place through the application of image-guided or computer-guided techniques to the current paradigm.

1.2 Image-Guided Surgery (IGS)

Minimally invasive surgery (MIS) techniques were first used on human patients in 1910 where laparoscopic exploration was used to assess for cancer in 17 patients [45]. The term MIS is used to broadly describe an array of medical techniques that reduce patient trauma while still achieving successful results. Reduction is trauma is

often accomplished by only using small ports into the body from which tools are fed; a camera or imaging system provides visualization instead of having a direct line of sight. Since the first laparoscopic exploration, MIS has improved healing times and reduced complications; however, MIS has a reduced amount of information available to the clinician due to reduced access. The interventional cardiology transcatheter closure of septal defects is an example of MIS as patient trauma is reduced when compared to the traditional open-heart methods. As transcatheter closure relies on fluoroscopy it still carries risk due to radiation exposure. Further solutions to risk from fluoroscopy that would offer not only dose saving to the patient but also the clinician should be explored.

Image-guided surgery (IGS) uses preoperative or intraoperative images are used in conjunction with localized surgical tools to provide the clinician tool positions in an anatomical context. The general schema for IGS procedures is the capture of preoperative images, collection of tracker data, calculation of image space to physical space registration, and display of images to the clinicians with tool positions overlaid. MIS procedures rely on an imaging system to provide visualization of tools in an anatomical context since there is reduced patient access due to the nature of the procedure. When the IGS paradigm is applied to MIS procedures, the clinicians ability to see the location of tools in the context of the patients anatomy is restored. In addition to restoring the visibility of subsurface tissues, the use of IGS reduces the reliance on live fluoroscopy thus reducing radiation exposure to the patient and clinical staff.

Many modern IGS systems use a software application running on a computer, which is interfaced with a tracking system. Use of an IGS software system in interventional cardiology requires the use of electromagnetic tracking as no line of sight with catheters would be obtainable using an optical method. There are a number

of currently available systems from both industry and academia, each following the general IGS schema. Commercial systems include solutions from: Phillips (PercuNav), Medtronic (StealthStation), Pathfinder Therapeutics (Explorer), Accuray (CyberKnife), Biosense Webster (CARTO XP), and St. Jude (EnSite). These systems each have a specific surgical procedure or range of procedures for which they are designed none of which include CHD repair.

1.3 Radiation Risk

Interventional cardiology patient exposure to ionizing radiation carries significantly higher risk than clinicians as patients are in the direct path of the x-ray beam. A cumulative patient dose study across cardiology found that interventional and nuclear medicine procedures accounted for the highest levels of exposure per procedure [10]. Average cumulative lifetime exposure of cardiology patients over an average of 36 examinations was reported to be approximately 61 mSv. The highest percentage contributor to the imparted dose were arteriography and interventional procedures (45%), however only 12% of all examinations are of this type [10]. Lifetime attributable risk (LAR) of cancer serves as a metric for determining whether exposure to ionizing radiation results in increased cancer risk while accounting for patient characteristics. Age and gender also affect LAR, for example a 64-slice CT in a 20 year old woman would result in a 1 in 140 risk but would only be 1 in 5000 for an 80 year old man.

As LAR is age dependent, pediatric interventional cardiology procedures pose an even higher risk to patients. Lifetime attributable risk diminishes over time but if the initial exposure was during childhood, significant risk would still persist well into adulthood. Along with having an increased sensitivity to radiation, pediatric

patients also present significant complexities into procedures due to anatomical size, faster heart rate and the inherent variability in the location of congenital heart defects. These additional complexities result in longer procedure times, leading to higher effective dose among pediatric patients when compared with adults. Since pediatric patients typically have a longer period of life left following exposure there is more opportunity for cancer to manifest. Studies conducted on cohorts of children with congenital heart defects, in the interest of finding a correlation between cumulative effective dose and chromosomal DNA damage, and have concluded that ionizing procedures cause long-lasting damage to chromosomal DNA [9, 7]. Using the observed chromosomal DNA damage as an indicator of LAR it was found that a male 1 year old child from the study had an excess risk of 1 in 352 while females had 1 in 156. Lifetime attributable risk in females is higher due to the radiological sensitivity of breast tissue [1]. Such LAR values raise concern when considering that cancer risk increases over lifetime, putting exposed children at higher risk than their healthy counterparts [2].

Motivation for the study of the cumulative dose effect on LAR and chromosomal DNA damage stems from a research call from the Committee on Biological Effects of Ionizing Radiation (BEIR) [55]. Several research needs are listed in the BEIR VII Phase 2 review, among them are further studies investigating low dose radiation effects on adults and children as well as further evaluation of epidemiological effects of radiation dose. Widespread concern over the effects of medical ionizing radiation especially on children serves as one of the primary motivations for this work.

A study conducted on clinicians evaluated the relationship between working in a cardiac catheterization laboratory and cancer risk, interventional cardiologists had the highest levels of exposure amongst other medical users of x-rays [69]. A second study, also on clinicians, showed that interventional cardiology procedures resulted in

an average occupational exposure of 1.6 mSv/yr while others have reported values as high as 4 mSv/yr [68, 50]. Even though these values are well within the maximum annual dose limit of 50 mSv and five-year average of 20 mSv/yr, radiation dose is cumulative over lifetime [1, 17]. Interventional cardiologists are especially at risk of developing cancer attributable to occupational radiation exposure due to heavy reliance on ionizing radiation and the number of procedures conducted each year which averaged 200 50 per clinician in 2008 [13]. Over an interventional cardiologists professional career (11-26 years), the range for occupational radiation exposure would be 17.6 – 41.6 mSv resulting in a range of approximately 33 to 79 cases of cancer amongst interventional cardiologists who numbered 6500 in 1997 [42].

Solutions to lowering the use of fluoroscopy in interventional procedures has been mainly focused around the use of dose saving devices and supplementation with ultrasound imaging. Among the techniques used for dose reduction are application of spectral filters, frame rate reduction, and patient specific tuning of X-ray parameters such as tube-voltage [70]. In addition to technical adjustments to cardiac catheterization procedures, methods such as increased radiation safety training and intra-procedure notifications of dose have led to further reductions [41]. While dose saving has seen success in reduction of patient dose by 30% to 50%, dose levels are still high enough to warrant the need for mitigation of the issue [47]. Supplementation of fluoroscopy with transesophageal echocardiography (TEE), an ultrasound based technique, is only a partial solution due to poor visualization when not in immediate proximity of the catheter. The quality of the images produced by the fluoroscope is greater than that produced from TEE resulting in limited use of TEE during procedures where radiation is not contraindicated.

Over the past two years we have been developing our novel image-guidance system known as Kit for Navigation by Image-Focused Exploration (KNIFE) to serve

as the IGS software system to be used for guidance of catheters during pediatric interventional cardiology procedures, more specifically ASD repair. In the development process, we have taken steps to make our system extensible and adaptable to other medical procedures. Preliminary work using KNIFE has generated enough data to validate its use in procedures with optically tracked medical instruments and magnetically tracked catheters such as the ones developed in this work. The extensible nature of KNIFE makes it a perfect candidate for the development of specific modules that will facilitate image-guided ASD repair in pediatric patients.

Chapter 2

Development of a Novel Image-Guided Surgery System with an Open Framework

2.1 Introduction

Minimally invasive surgical (MIS) techniques improve healing times and reduce patient trauma but also limit surgical access, which can make a procedure more difficult. Image-guided surgery (IGS) provides surgeons with positional information, which can in-part replace the data lost in MIS by using medical images as a map to anatomic structures. The first image-guided procedures were in the field of neurosurgery, in these cases a radiolucent stereotactic frame was attached to the skull and used for positioning [33]. In these early techniques, the patient would have a CT scan with the frame attached and tools would be aligned to the images based on the geometry of the frame, allowing the images to be used to target diseased tissues [27]. Stereotactic neurosurgery proved cumbersome for both the patient and clinician due

to the size and weight of the frame and the requirement of it being attached during imaging and surgery. Frameless, interactive IGS systems were developed to reduce the need for large, cumbersome equipment, allowing for real-time display of surgical tools on preoperative or intraoperative images.

The first interactive IGS systems used articulating arms to calculate the position of a stylus positioned at the end effector, the position of the stylus was then overlaid onto preoperative tomographic images [37]. As the performance to price ratio for computational equipment has raised more sophisticated IGS systems were developed. Systems built using normal desktop PCs with multiple processors were built and in some cases multiple articulating arms were used to track multiple tools. The introduction of tracking technologies allowed for replacement of the articulated arms in favor of tools that could be directly tracked. The first tracking systems used in IGS were optical trackers, which used triangulation for tool localization, in the same way as surveying equipment localizes. With the development of Digital Imaging and Communications in Medicine (DICOM) standard format for image storage and transmission a standardized method of loading image data has become available, which is cross-modality and cross-manufacturer. The DICOM standard has made it easier for medical imaging software to interact with captured images, thus making it possible for IGS systems to directly load images without handling vendor specific file formats.

At the center of an IGS system is a software package that takes in tracker data, performs image space to physical space registration, and displays the images to the clinicians. There are a number of currently available IGS systems from both industry and academia, each following the general IGS schema. Some of the current IGS research systems such as the Operating Room Image-Oriented Navigation (ORION) system use a modular approach based on dynamically linked libraries (DLLs) to

facilitate usage in a wide breadth of settings [65]. The ORION system takes the format of a closed source, open architecture package; allowing the end-user to add new modules, but not modify the actual central application. Development of toolkits such as the image guided surgery toolkit (IGSTK) use an open source C++ object oriented approach to allow for quick development of specialized IGS software systems [28, 21]. IGSTK allows for modulation of the overall system using a widespread development approach. In this approach, a large community develops source code and submissions of this code to the core code base are overseen by a small group of project leaders. This method of development has been proven useful in many projects but has led to issues regarding code maintainability and consistency amongst users. Even with these concerns, IGSTK has seen widespread usage in the research community as it allows for high-level programming of common image-guided surgery application functionality.

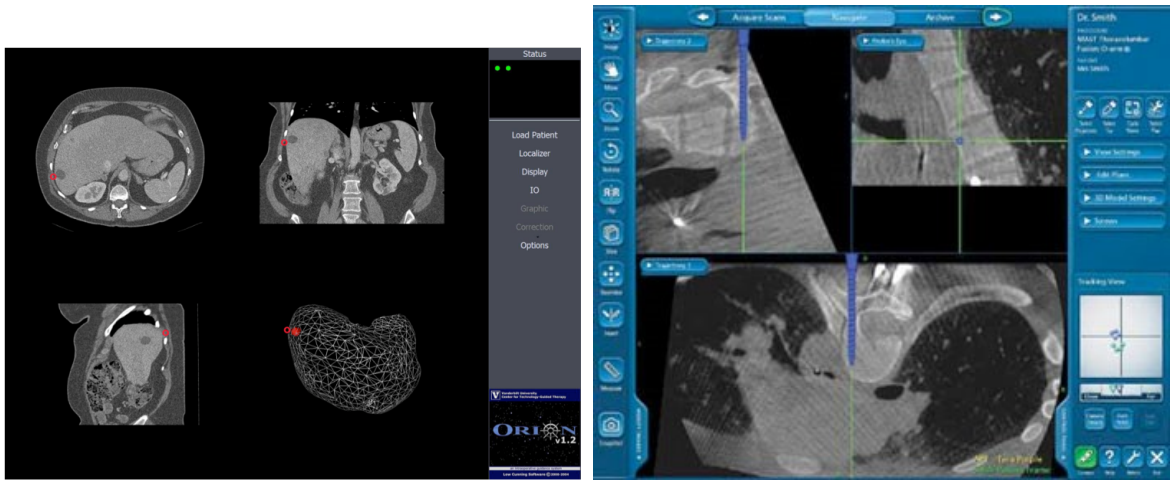

(a) Orion (b) Stealth Station

Figure 2.1: (a) Screenshot showcasing the general display of the Vanderbilt University SNARL developed image-guided surgery software ORION. (b) Medtronic's Stealth-Station software displaying an image-guided pedicle screw insertion procedure. The software is able to assist in planning and placement of each screw.

Database in Real-Time (FINDER) (Mayo Clinic, Rochester, MN) system utilizes a distributed computing approach in which multiple computers are used each with a specific task within the image-guidance schema [60]. FINDER facilitates communication between several computers each assigned a specific task or set of tasks, through a centralized database and messaging system. Each of these systems takes part in the overall workflow and in the presentation of data to clinicians. Inherent issues in the design include latency of triggered events as well as the overhead associated from purchasing and maintaining the various systems required for operation. One last notable research IGS system is the 3D Slicer that is built using the NA-MIC kit which itself is a collection of other toolkits and software libraries [29]. 3D Slicer implements the standard IGS system features but is also capable of image processing and interactive visualization of volumetric datasets. It has enjoyed widespread usage in medical imaging computing and visualization but has not seen extensive usage in IGS procedures. While rich in features, 3D slicer is built upon code that has not been verified and validated preventing it from being approved for clinical use.

We have developed a novel image-guided surgery system drawing from the strengths of previous systems and using modern techniques to add new useful features that will speed up research development times. Initially, the IGS software suite was designed and developed to support catheter guidance procedures for the repair of atrial septal defects. While a specific application was in mind for the software, an application agnostic approach was used. The reasoning behind this decision is two-fold: first, an extensible platform would allow transition to other vascular procedures in the future; second, having an open system without any hard-coded features would allow future developers to integrate features not considered or available during the original development timeline.

2.2 Methods

Development of our image-guided surgery software suite was an iterative process where the core code base was refactored or restructured on multiple occasions. Ultimately, the current design proved to be the most stable while still adhering to the original design goal of being user-extensible. Our approach is best described as a software architecture designed around a set of user-supplied core modules allowing for the compartmentalization of subsystems within a larger application framework. All together the software is a set of utilities for developing custom image-guided surgery components without the need to create aspects that are not central to the research goal. We refer to our IGS software framework as Kit for Navigation by Image-Focused Exploration (KNIFE) because it aptly describes its primary use. KNIFE consists of two separate code bases, the KNIFE application, and the KNIFE software development kit (SDK). The KNIFE application is a windows program, which uses the native Windows-32 SDK and the KNIFE SDK as central frameworks.

2.2.1 KNIFE SDK

The KNIFE SDK is an image-guided surgery framework that allows for the easy development of image-guided surgery applications. Included in the framework are several sub-libraries that facilitate the loading and display of medical (DICOM) images, connecting to tool localizers, registration of coordinate systems and a plugin system. KNIFE SDK provides several singleton controller classes that are used to organize and hold persistent memory objects pertaining to a subsystem. A class in the C++ programming language is a data structure that contains functions and relevant member variables defined by the programmer. The manner by which a class is designed can enforce desirable features which in the case of a singleton class, permits

creation of only a single instance or object of the class. By allowing only a single object of a class to exist at program runtime, issues related to multithreading with shared data can be effectively mitigated. In the case of the KNIFE application where multiple concurrent threads are used to provide processing speed gains, direct control over data access prevents situations where a variable is changed by one thread while being read by another. This can lead to unpredictable results as the flow of the program is determined by which thread accesses the variable first which is unknown to the programmer.

There are eight controllers in the library ranging from DICOM image administration to plugin object handling. KNIFE SDKs controllers form the core of the library and the functionality they expose allows for the development of custom user modules that can change the functionality of the system. The tracker, registration, and graphics controllers contain a pointer to an interface object that allows for extensibility of core functionality in the controller. These controllers are referred to as empty controllers as the core functionality that they provide is through user generated portable DLL code libraries. By establishing a common C++ interface for these core subsystems, it is possible to create a framework of functional building blocks that can be used by researchers to create personalized versions of an IGS system.

2.2.1.1 Digital imaging and communications in medicine (DICOM)

Modern medical imaging systems capture images and store them with relevant metadata in an industry standard file format known as Digital Imaging and Communications in Medicine (DICOM) [4]. This metadata contains all relevant patient data, acquisition parameters, and processing and visualization data. Information from the metadata in the DICOM files is incredibly useful in an image-guided surgery setting. When loading DICOM files, the KNIFE SDK makes the metadata within image files

available to the entire plugin system thus allowing the implementation of algorithms without requiring user input. A plugin developed for simplifying the registration process is able to retrieve values for image pixel spacing allowing for the conversion of unit-less image pixels to physical distances in fiducial location collection.

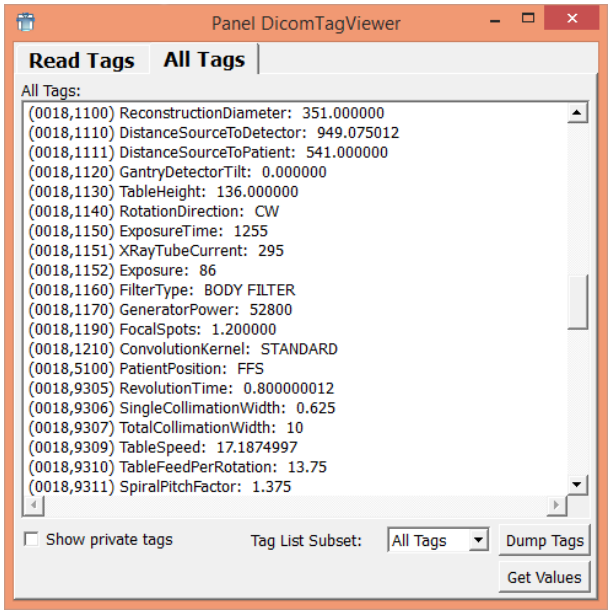

Figure 2.2: Display of DICOM metadata from a CT image data set using the open-source software MevisLab. Each tag has a name and an expected data type for use in retrieval from the stored image file.

KNIFE SDK is able to interface with DICOM files through the usage of the DICOM Toolkit (DCMTK) C++ library which has over 19 years of development and implements the most comprehensive amount of the DICOM standard [67]. The KNIFE SDK does not simply wrap the DCMTK library; extra functionality is added to the built-in abilities, through KNIFE SDK internal classes. Inclusion of an interface with DICOM files was a design priority as every medical imaging system can output such files and this would eliminate the need for doing vender specific image-preparation steps. Additionally, having direct DICOM support also allows for run-time loading and unloading of images to save application memory.

Extension of the functionality of DCMTK wrapped in KNIFE SDK is accomplished through the implementation of helper classes. Helper classes ranging from loading DICOM files from a DICOMDIR, a directory hierarchy index file, to providing an easy to use DICOM file object were created. A readily available DICOM interoperability API that exposes information in DICOM files has allowed for the development of image processing, metadata information display, and file hierarchy traversal plugins without direct user intervention. By including intuitive DICOM classes we are able to free the developer from dealing with code that is not specific to their application. Other image-guided surgery systems require pre-processing of image data prior to use, which results in an intermediate step that often requires additional software and user time. The extensible design of KNIFE attempts to create a software environment where procedure-planning steps such as tissue segmentation can be accomplished without leaving the IGS software. This can lead to more streamlined IGS procedures where changes to the visualized data can occur in real-time since the data was originally generated in KNIFE.

2.2.1.2 Tool Tracking

A key component of every image-guided surgery system is a tool localizer. Tool localizers vary in the tracking technology used to determine the position of objects within some geometric volume. The two most commonly used technologies for tracking tool positions are optical tracking and electromagnetic tracking.

Optical tracking relies on position sensors attached to tools in order to produce a location transform. There are two types of position sensors, passive and active, where the former uses reflected light from the tracker cameras and the later emits light to indicate position in the volume. While optical tracking can offer submillimeter accuracy, line of sight is required to determine a position. Since tools such as catheters

(a) (b)

Figure 2.3: Optical (a) and electromagnetic trackers (b) from Northern Digital Inc., each technology offers differing levels of accuracy, tracking volume and line of sight leading to adoption based on procedure requirements.

enter the body and cannot be seen, they will not be able to be tracked using optical tracking technology.

Electromagnetic tracking uses a magnetic field generator emitting low intensity varying fields to create a volume to track small sensors. Sensors for EM tracking can be embedded in tools and placed out of line of sight while still being able to be tracked. This makes it possible to place sensors in needle tips or even catheter lumens and retrieve the position of the sensor in the volume of the field generator. Sensor locations are determined by the characteristics of the current induced in the sensor dependent upon angle and location from the field generator. While EM tracking does not require line of sight, the accuracy can vary dependent upon presence of ferromagnetic materials or objects of large mass in the environment, which can have lethal outcomes in medical uses.

KNIFE SDK implements a C++ interface that provides a skeleton for creating

a KNIFE localizer/tracker module. An interface approach allows for any application developed around the KNIFE SDK to use any tracking system. The virtual functions required for implementation provide a guideline on how to set up a tracker control library. By establishing a common structure for development of tracker controllers there will be less code redundancy decreasing development times. Currently there are two tracker modules written for KNIFE: one for the NDI Polaris optical trackers and one for the NDI Aurora EM tracker as seen in figures 2.3a and 2.3b. These two trackers are used since they are readily available to our lab and are industry standards being included in many commercial IGS systems for tool tracking.

Localizer manufacturers often include an API that can be used to query tool locations from a system control box. The system control box contains the necessary hardware and software to determine the location of a tool within the tracking volume. Tracking volumes can be generated by a field generator in the case of electromagnetic tracking or can simply be the viewing volume of a stereoscopic camera setup, such as is implemented in the NDI Polaris. By wrapping the manufacturers API in the KNIFE tracker abstraction class, we are able to provide tracker integration through a common class structure that is agnostic to the tracker hardware used.

2.2.1.3 Graphics

An image-guided surgery system must have the ability to create a combined representation of surgical tool locations and medical images that can be presented to the clinician for tool guidance. KNIFE SDK offers a convenient wrapper around the industry standard OpenGL graphics rendering API offering functions for drawing basic primitives, 2D images and 3D or volumetric data sets among many more. These functions collectively form a barebones graphics toolkit that can be used in the absence of other more feature rich toolkits. Every PC has an implementation

of OpenGL, which is included with graphics drivers and the computers operating system. OpenGL has an advantage over a graphics API like DirectX in that is not a traditional API but instead is an API specification that graphics hardware manufacturers implement in their own drivers. By serving as a specification rather than a fully featured API, OpenGL can be implemented on any operating system and is already included in Windows, OSX and Linux.

Since OpenGL is implemented by the graphics card manufacturer, the function calls are optimized for the hardware yielding higher performance than when using other low-level graphics libraries. Pre-developed graphics libraries such as Visualization Toolkit (VTK) and Open Inventor were not used in the KNIFE SDK to allow the developer to use any library in their own implementation of the graphics interface. This approach allows for the development of KNIFE SDK wrappers for any existing graphics toolkit or API giving the user the freedom to use the library they are most comfortable with. IGS software systems are typically paired with a specific hardware set and the building block style of the KNIFE SDK architecture allows for system level optimizations increasing performance for graphically intensive tasks.

The portability and speed of OpenGL code made it a great choice as the backend rendering API for the KNIFE SDK. If the developer has no need for a specialized rendering module there are two included, one that handles 3D image volumes such as CT or MRI and another that handles 2D image sets such as planar x-ray or ultrasound. Several functions exist for drawing shapes and objects to the rendering window, which are extensively used in displaying tool locations and creating complex displays such as catheter shape. The graphics controller in KNIFE provides several callback hooks that a user can subscribe to permitting the use of an event driven approach in plugin development where a user function can be called after images are rendered or when a user clicks an image.

2.2.1.4 Registration

To accurately represent tool locations on the preoperative images, a transformation matrix is used to convert reported tracker locations to the coordinate space of the images. The transformation matrix encapsulates all linear 3D transformations that are required to achieve the best fit between the tracker and image coordinate systems. A transformation that is strictly linear is typically obtained from a rigid registration algorithm, where one or more transformations may be required before achieving an optimal fit. A quick and simple algorithm used is Procrustes analysis, where corresponding points in two coordinate systems are used to find the required linear affine transformations to achieve the best possible fit between the coordinate systems. We have currently developed a KNIFE registration module that takes corresponding points on a physical model and its image representation and outputs a 4x4 transformation matrix that can be used to convert incoming tracker points to image space.

The registration controller in KNIFE defines an interface that can be used to develop custom registration modules for use in IGS research. Design of the registration module interface is simple requiring implementation of a single function that houses the logic for the registration algorithm. This register function is the access point used by other components of the SDK to perform a registration between collected point sets through the use of API functions. Once a registration is complete, the resultant transformation matrix is stored in the DICOM image object in memory and a flag is set that allows all registration dependent code to run safely. Using this approach we are able to abstract away the registration algorithm allowing for separate development by algorithm designers without the need to develop the rest of the IGS system.

Each registration module is required to return a metric of the level of fit obtained from the registration algorithm. This level of fit is known as the fiducial registration error (FRE) and is a measure of how well a transformed point represents the actual location. Safe FRE values are procedure dependent where for a liver surgery a few mms would be tolerable but in a heart procedure, less than 1 mm could mean missing a target. Level of fit values returned can be used to determine if the registration is usable for the given procedure or if another registration should be performed.

2.2.1.5 Plugins

A central design goal of KNIFE is extensibility, and this is accomplished through encapsulated code libraries or plugins that implement a predefined interface. The provided interface class serves as the common communication gateway between the KNIFE SDK and the functionality in the plugin. An interface approach instead of a set of exported functions allows the developer to use an object-oriented approach in their design. This approach also provides a simple wrapper that is useful for when plugins need to interact at runtime. Plugins serve as separate code libraries that interact within the run-time memory of the KNIFE application. Functions in the KNIFE SDK that change DICOM data require user confirmation and plugin encapsulation enforces this as KNIFE is able to identify which plugin is requesting to perform a certain action. The developed plugin system provided in the KNIFE SDK can be used in a new application or can be used in the existing KNIFE application.

2.2.2 KNIFE

Using the developed KNIFE SDK and other external libraries a Windows application was created that is referred to as KNIFE. This application uses modern programming principles such as multithreading as well as implements the full feature set of an image-guided surgery system. Development of KNIFE occurs in tandem with the KNIFE SDK and serves as a means of testing newly implemented features. The KNIFE codebase consists of a mixture of legacy C code interacting with C++ classes due to the requirements of libraries such as Win32 which is entirely written in C [53]. Program user interface (UI) is accomplished through the use of the Win32 library wrapped in custom classes which results in organized and manageable code that can be extended with minimal detriment to already developed code.

A wizard which guides the user through the selection of DICOM files and appropriate modules is included in KNIFE (Figure 2.4). The wizard is used to load a study into the KNIFE software allowing for users to setup a new procedure in a simplified manner. Once the user reaches the final step of the wizard all images are loaded directly into memory, modules register with their respective controllers and plugins are initialized. If the user already knows which objects need to be loaded a custom study file known as a KNIFE Startup Script (KSS) can be created which will cause KNIFE to automate the process forgoing the need to traverse the wizard. A KSS file consists of tags followed by values which KNIFE parses if a file is provided at program startup. Once a study is fully loaded the user is responsible for tasks such as initializing localizers, registering coordinate systems and running of plugins.

Graphical displays in the KNIFE application include a 2D image viewer defaulted to a quad configuration but has functionality for single and dual views. Each sub-window in the 2D viewer is running on a separate thread and implements the call-

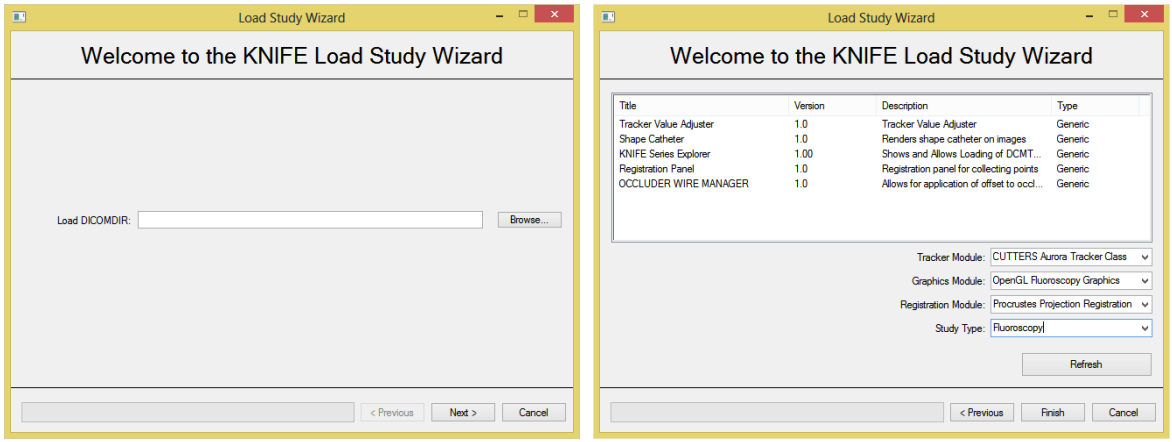

(a) (b)

Figure 2.4: Screenshot of KNIFE load study wizard steps demonstrating how users are guided through the process of setting up a new procedure.

back functions included in the KNIFE SDK allowing for plugins to overlay graphics on the underlying medical images. An example of such use is the display of tracked tool locations on images during IG procedures. By providing each window its own thread we are able to prevent any one subsystem from halting the full application. This is an important feature as the computational requirements of future developers is not known and a system with a single threaded queue could become unusable for computationally demanding applications. Another notable feature of the 2D viewer window is the inclusion of a user customizable fourth window that operates separately from the graphics module. This fourth window can be controlled by plugins to provide additional graphical views or textual information. A screenshot displayed in figure 2.5 shows the 2D viewer in dual image mode with supporting plugin windows surrounding it. A window for viewing 3D image datasets exists but its use is limited as the KNIFE SDK has not yet fully implemented its required features.

Constant communication with the attached localizer is also accomplished using a separate thread. A custom designed message pump is used which involves collection of new tool locations, transformation to image space, followed by insertion

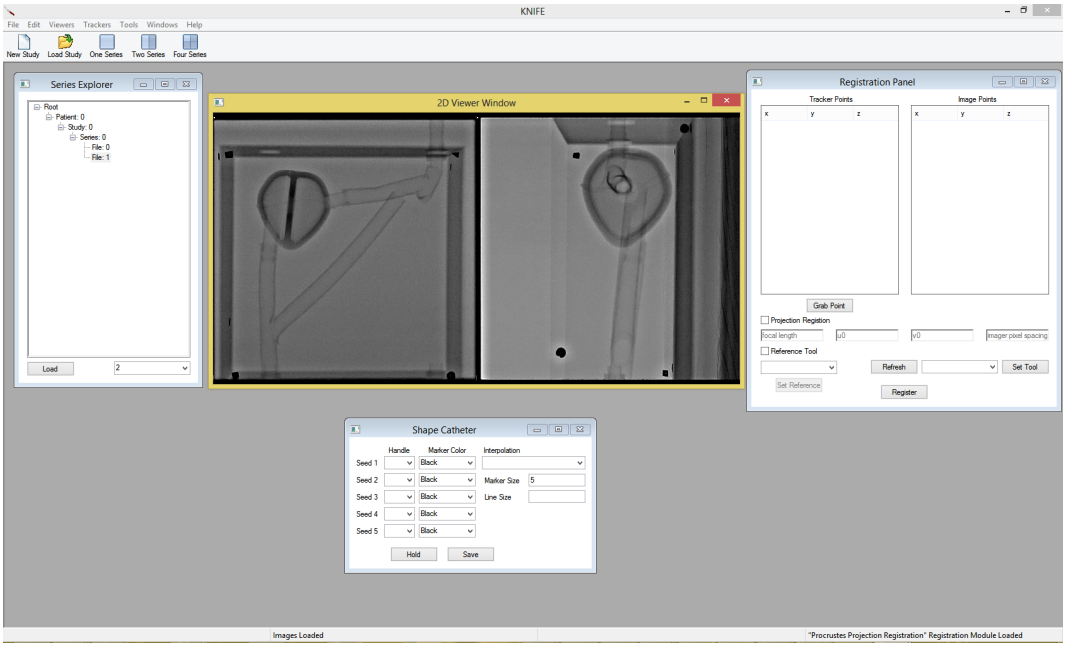

Figure 2.5: Screenshot of KNIFE displaying a bi-plane fluoroscopic image set with windows from loaded plugins surrounding it.

into the provided KNIFE SDK data structures. Each iteration of the pump provides all attached KNIFE plugins with updated tool locations in both localizer and image coordinate spaces without the need to query the localizer directly. Using this design significantly speeds up program execution allowing for full capture of each produced frame from the localizer which is running at 40 Hz.

2.3 Discussion and Conclusions

Over the course of KNIFEs development it was adapted and used in multiple research settings where the demands for each procedure differed serving as a general means of validating KNIFE as an IGS system:

One application of the KNIFE IGS framework is in interventional cardiology where electromagnetic (EM) tracking seeds are embedded in the lumen or fixed on

the outside of catheters and used in cardiac catheterizations. Repair of defects resulting from congenital heart disease (CHD) is the main focus of the research with atrial septal defects (ASD) being studied initially. The current system is capable of displaying the tip of the catheter on a pre-captured fluoroscopic image loop. Initial results revealed a significant ($p < 0.05$) reduction in radiation dose while using KNIFE guidance in comparison to fluoroscopy guidance alone. Currently this work is progressing towards the construction of multiple tracking seed catheters to capture shape and the development of novel techniques for integrating IGS into CHD repair.

Another such adaptation is an image-guided diagnostic biopsy system that is currently being developed around the KNIFE SDK with functionality to record the position of core samples. Design of this new IG system includes the display and augmentation of pre-procedure 3D image sets with 2D images captured during the procedure. Using the perceived augmentation it is theorized that a higher accuracy in location recording for each biopsy sample can be achieved. Additionally, augmentation of the initial image set will allow for real-time image update adding physiological dynamics into the IG procedure providing a more accurate representation of the target anatomy.

KNIFE has reached a stable development point and has already seen usage in research settings where favorable results were obtained. As KNIFE becomes used more often, the core codebase is expected to adapt and popular plugins will be incorporated into the SDK. Further development will be focused around maintaining, cleaning and documenting the existing codebase to ensure that future developers can continually update the project.

Chapter 3

Assessment of Accuracy and Distortion in Fluoroscopy for use in Image-guided Surgery

3.1 Abstract

This manuscript assesses the accuracy and the distortion of fluoroscopic images with the goal of determining whether usage of these 2D images is justifiable in image-guided procedures where position within a 3D volume is tracked and overlaid onto an image set.

Intrinsic parameters (principal point and focal point) of the fluoroscope were quantified using an automated technique based on a 3D grid calibration phantom. Error attributed to perspective projection distortion was measured using the calculated intrinsic parameters of the fluoroscope and the segmented centroids of the points in the fluoroscopic images. A second grid phantom was traversed through the fluoroscopic imaging volume of an image intensifier and solid state system at 2 cm intervals,

building a scatter field to demonstrate projection. Centroid grids of a single plane from each scatter field were used to measure and demonstrate pincushion and 'S' distortion. Effects of projection distortion on the images was assessed by calculating the RMS directional error between each point and an ideal world representation of the 3D grid phantom. Ordinary Procrustes analysis was used to align the coordinate systems of the various point clouds so alignment error could be assessed. A case study was performed to test whether transforming image points to camera space results in a better registration in a mock scenario.

Images and directional error collected of the 3D grid phantom revealed lower error in the alignment between camera and world points than image world points. Qualitative data collected for both phantoms indicated that flat panel fluoroscopes have lower error than their image intensifier counterparts. RMS directional error for each 2D centroid grid showed a clear difference between the error for flat panel and image intensifier fluoroscopes.

The data demonstrates that projective transformation of image points to camera space is essential to finding a registration that has lower error. Results proved that flat panel fluoroscopes capture less distortion than image intensifier systems and should be used to capture images that are intended to be used in image-guided procedures. Use of fluoroscopic images from flat panel systems coupled with transformation of points into camera space is crucial to minimizing the amount of error introduced into an image-guided procedure.

3.2 Introduction

Fluoroscopy has been applied in real-time diagnostic and interventional procedures since its invention shortly after the discovery of the X-ray [61]. Fluoroscopy

has successfully advanced minimally invasive interventional procedures as it provides a means to see into the body, thus allowing visualization when the clinician has no line of sight. Initial fluoroscopic systems relied on a standard scintillator without any recording method, and without any secondary gain requiring clinicians to dark adapt prior to viewing the resultant low brightness images. Progress in technology yielded the Image Intensifier (II) which produced a brighter however minified version of the image. The II revolutionized the fluoroscope, allowing clinicians to view captured images without the need for dark adaptation.

Introduction of the first solid state detector fluoroscope in 2001 further revolutionized the modality, replacing the image intensifier, video camera, digital spot film device and the cine camera of the fluoroscope [18]. Fluoroscopes that utilize solid state detectors are referred to as flat panel fluoroscopes since they lack the curved phosphor screen of the II. Replacement of large parts by the solid state detector allows flat panel systems to be smaller and lighter than vacuum tube based II systems. In addition, solid state detectors do not require a vacuum environment, have dynamic pixel sizes and have better quantum detection efficiency than that of the II [12].

3.2.1 Geometry of the Fluoroscope

Fluoroscopy is a projective imaging modality where 3D objects are compressed into a 2D image at the imaging plane which is then recorded by the image intensifier or solid state detector. This imaging plane can be assumed to be the focal length away from the x-ray source [74]. The transformation of the 3D space into 2D images occurs through a perspective projection transform whereby objects closer to the x-ray source appear larger due to magnification, while objects closer to the detector will appear closer to their normal size. In this captured perspective projection, distances

and angles between objects are not preserved unless they are on the same plane along the projective axis. A generalized transformation of 3D world points to 2D image points can be represented as:

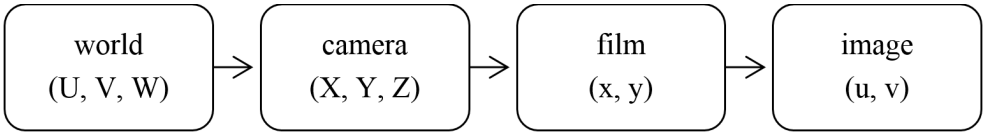

Figure 3.1

Mapping of a world point $P_{World} = [U\ V\ W\ 1]^T$ to an image point $P_{Image} = [u\ v\ 1]^T$ is accomplished through a 2D-3D transformation matrix T_{2D-3D} composed of three matrices, a film matrix T_{Film}, a projection matrix $T_{Projection}$ and a rigid body transformation T_{Rigid}:

$$T_{Film} = \begin{bmatrix} \frac{1}{s_x} & 0 & 0 \\ 0 & \frac{1}{s_y} & 0 \\ 0 & 0 & 1 \end{bmatrix} \tag{3.1}$$

$$T_{Projection} = \begin{bmatrix} k_u & 0 & u_0 & 0 \\ 0 & k_v & v_0 & 0 \\ 0 & 0 & 1 & 0 \end{bmatrix} \tag{3.2}$$

$$T_{Rigid} = \begin{bmatrix} \cos\beta\cos\gamma & \cos\alpha\sin\gamma + \sin\alpha\sin\beta\cos\gamma & \sin\alpha\sin\gamma - \cos\alpha\sin\beta\cos\gamma & t_x \\ -\cos\beta\sin\gamma & \cos\alpha\cos\gamma - \sin\alpha\sin\beta\sin\gamma & \sin\alpha\cos\gamma + \cos\alpha\sin\beta\sin\gamma & t_y \\ \sin\beta & -\sin\alpha\cos\beta & \cos\alpha\cos\beta & t_z \\ 0 & 0 & 0 & 1 \end{bmatrix} \quad (3.3)$$

$$T_{2D-3D} = T_{Film} T_{Projection} T_{Rigid} \quad (3.4)$$

Where s_x and s_y are the pixel size in mm in the x and y axes respectively and k_u and k_v are the focal length (f) divided s_x and s_y. Parameters u_0 and v_0 are the location of the point through which a vector drawn from the center of the x-ray source passes through the image plane or the principal point. α, β, γ are the angles of rotation about the x, y and z axes respectively and t_x, t_y and t_z are the translation in the x, y and z directions respectively. The T_{Film} matrix describes the transformation of objects captured by the camera into image space. Values for the focal length, u_0, and v_0 are found by calibrating the fluoroscope using the method presented later in this paper.

Advancements in fluoroscopic technologies have not come without a cost. Image intensifier systems are known to introduce 'S' distortion and pincushion distrotion which are caused by the earth's magnetic field and the curvature of the input phosphor of the II [15, 14, 77, 58, 64]. Error in flat panel systems has not been investigated to the knowledge of the authors. We believe that due to the physical mechanism by which fluoroscopic images are produced, there is still a certain degree of error in the represented locations of objects in images even with solid state equipment. For

typical fluoroscopy guided procedures, this error has become non-issue as the visual representation of tools in the images is also distorted. Clinicians often align the center of the fluoroscopic volume with the anatomical region of interest since fluoroscopic systems are calibrated and focused at the center of their imaging volume. Issues with image quality and incurred error become important when fluoroscopic image sets are used in Image-Guided Surgical (IGS) procedures.

3.2.2 Image-Guided Surgery

In IGS procedures a pre-procedure image set is collected and registered to the coordinate system of a spatial tracking system, thus finding the transformation between the imaging device and the physical world. Procedure tools, such as scalpels, catheters, and probes, are spatially localized using the tracking system, with position being reported in the tracking system's coordinate space. The registration provides the mapping between coordinates in tracker space and image space. This registration between the two coordinate systems implies that the locations have a direct correspondence. There is an assumption that both the tracking system and the imaging system are accurately reporting the spatial position of tools and objects respectively.

When applying coordinate transformations in IGS procedures, the world space is most often represented by the volumetric space reported by the tool tracking system. Objects in the world coordinate system are automatically converted to objects in the pixel coordinate system based on the extrinsic and intrinsic properties of the imaging system. The extrinsic properties constitute a rigid body transformation of the world to the camera space which can be found using a registration algorithm such as rigid Procrustes analysis. Intrinsic properties of the camera include values such as the incident point (u_0,v_0) and the focal length (f).

Accurate reporting of locations in fluoroscopic images relies on the intrinsic properties of the x-ray source and detector. In II systems, distortion is incorporated into the output images, leading to varying amounts of error throughout recorded images. In general, there are two sources of geometric distortion in II systems: pin-cushion distortion and transient 'S' distortion with certain regions having larger amounts of error. Pin-cushion distortion is caused by the curvature of the input phosphor of the II. Transient 'S' distortion is caused by the earths magnetic field resulting in inaccurate reporting of distances in images [63]. These distortions have been overcome in flat panel detectors but the images still suffer from perspective-projection distortion which occurs due to differences in depth along the axis of the x-ray source [32].

Numerous studies have investigated the use of the fluoroscope in IGS in a variety of different configurations. One study looked at fusion of 3D fluoroscope images and preoperative CT volumes [71] while others used image processing techniques to localize tools in captured images [23, 76]. Studies have shown the use of electromagnetic tracking with position overlaid onto fluoroscopic images [39] as well as motorization of the fluoroscope [66]. Work involving the use of fluoroscopic images to select targets that will be overlaid onto an endoscopic video feed has established that reduction of error in the collected images is necessary prior to their use in IGS procedures [73]. In this work, we aim to investigate the error incurred by fluoroscopic images due to perspective-projection distortion in the fluoroscopic imaging system.

3.3 Materials and Methods

The spacial error in fluoroscopic images must be quantified in order to use them in an image-guided procedure. Methods have been explored towards mitigation

of II based distortion through the development of solid-state detectors, at this time however, widespread propagation of the technology has not yet been achieved. In this study we have established a method for the automatic estimation of the intrinsic properties of the fluoroscope and have explored distortion effects in fluoroscopic images from both II and solid-state detector systems. The impacts of this distortion were assessed to determine the feasibility of image-guided atrial septal defect (ASD) repair.

3.3.1 Automated Estimation of Fluoroscopic Intrinsic Parameters

Intrinsic parameters of the fluoroscope, principal point (u_0, v_0) and focal length (f), were estimated using an automated calibration technique. Central to the technique are fluoroscopic images of a 3D grid phantom built with tight geometric constraints. Construction was accomplished through the layering of several 10 cm x 10 cm x 0.3 cm acrylic sheets each containing a different hole pattern cut by a laser-milling machine (Versalaser 2.30, Universal Laser Systems, inc., Scottsdale, AZ, USA). Lead BBs were placed in the holes at each layer to serve as markers for the calibration. Overall, the design generated a 3D phantom with markers at varying locations in all three planes allowing for constrained volumetric marker capture of the fluoroscopic imaging volume. The phantom was imaged using a Toshiba bi-plane Infinix-i series fluoroscope with solid-state detectors (Toshiba Inc., tawara-shi, Tochigi-ken, Japan) and a Ziehm Imaging II C-arm (Ziehm Imaging, Orlando, FL, USA). Images were captured with the phantom oriented to face the x-ray source in both the anterior-posterior (AP) and lateral (LR) planes for the bi-plane fluoroscope. Position of the phantom relative to the x-ray source and detector were recorded along with the cap-

tured images.

Automated calibration of the fluoroscope requires the use of the captured images, recorded distances and the geometric design of the 3D phantom. Since each marker completely attenuates the x-ray beam they are represented as dark circles on the captured image in Figure 3.2(a). A binary mask was created using a threshold value 5% lower than the max pixel value of the markers (Figure 3.2(b)). Connected-component labeling was used for the detection of individual markers in the image and the gray weighted centroid of each located marker was calculated (Figure 3.2(c)). Each marker was then assigned a location identifier based on its location in the phantom (Figure 3.2(d)). The location identifier is assigned based on the calculated neighbor count of each marker as well the location identifier of those neighbors. Each centroid location was then given a depth based on the assigned location identifiers and the recorded distance from the x-ray source (Figure 3.2(e)(f)).

The two equations for the finding the pixel location in perspective imaging are:

$$u_x = f\frac{X}{Z \cdot s_x} + u_0 \tag{3.5}$$

$$v_y = -f\frac{Y}{Z \cdot s_y} + v_0 \tag{3.6}$$

In equations 3.5 and 3.6, (u, v) is the image point in pixels and (X, Y, Z) is the camera point in millimeters. Since the true values for X and Y are unknown for each point, relative distances from other points can be used in determining the principal point (u_0, v_0) and focal length (f).

Assuming the marker in the top-left corner of the phantom to be the origin, distances for each marker from the origin were found. Utilizing the calculated distances from the origin, D_x and D_y, in the x and y direction respectively, the following sets of equations were used to find the fluoroscopic parameters using a multivariate

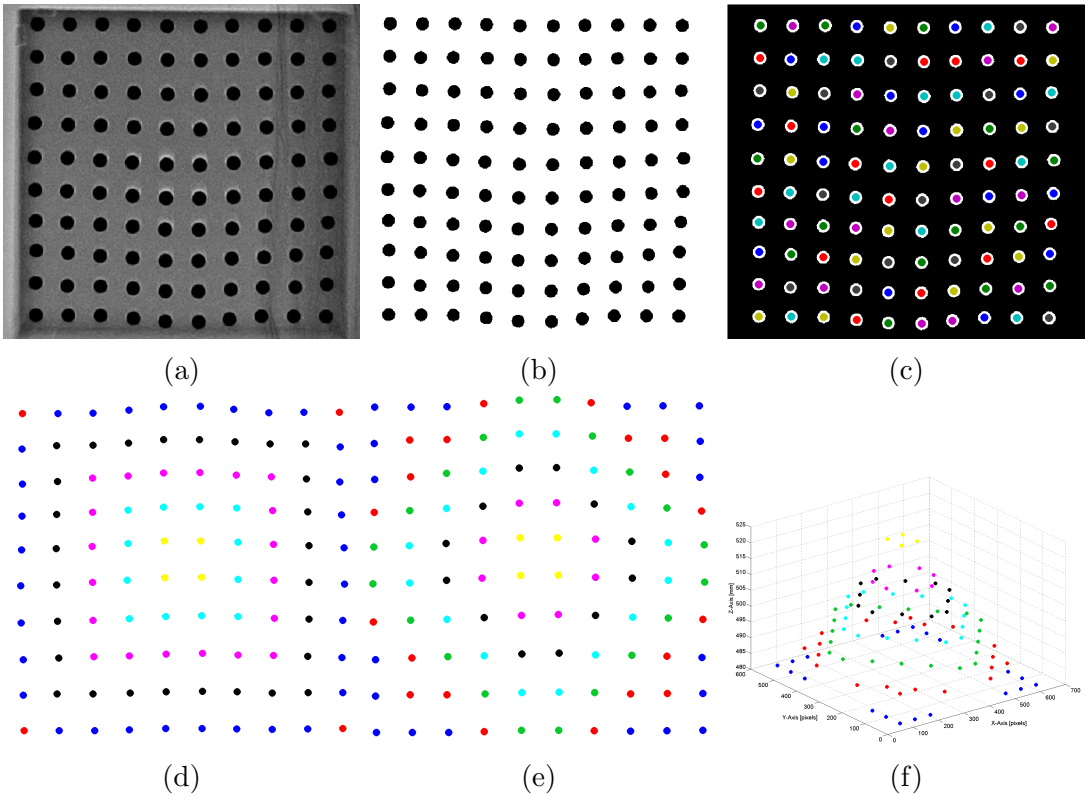

Figure 3.2: Overview of each step in the automated calibration technique for the lateral plane on the flat panel fluoroscope where BBs in the image are located and assigned their proper depth. (a) Original fluoroscopic image. (b) Post thresholding of fluorscopic image. (c) Connected component labels of BBs in image. (d) Centroid locations of each BB with color applied to signify different location assignments. (e) Centroid locations of each BB after depth has been assigned. Each color signifies a different depth. (f) 3D scatter plot of centroids extracted from fluoroscopic image.

linear regression in which the equation for each marker-origin pair was used.

$$X_{(0,0)} = X_{(n,n)} + D_x \tag{3.7}$$

$$Y_{(0,0)} = Y_{(n,n)} + D_y \tag{3.8}$$

$$X_{(n,n)} = \frac{Z_{(n,n)}}{f}[(u_{(n,n)} - u_0)s_x] \tag{3.9}$$

$$Y_{(n,n)} = \frac{Z_{(n,n)}}{f}[(v_0 - v_{(n,n)})s_y] \tag{3.10}$$

Equation 3.7 and 3.8 are the used to find the location of an adjacent point in both the x and y axes respectively. Locations of points can also be found using equations 3.9 and 3.10. By substituting equations 3.9 and 3.10 into equations 3.7 and 3.8 we can derive a general form to calculate the unknown intrinsic parameters of the fluoroscope.

$$D_x f - s_x u_0(Z_{(n,n)} - Z_{(0,0)}) = s_x(Z_{(0,0)}u_{(0,0)} - Z_{(n,n)}u_{(n,n)}) \tag{3.11}$$

$$D_y f - s_y v_0(Z_{(0,0)} - Z_{(n,n)}) = s_y(Z_{(n,n)}u_{(n,n)} - Z_{(0,0)}u_{(0,0)}) \tag{3.12}$$

Equations 3.11 and 3.12 were populated and used in the multivariate linear regression to find the maximum likelihood estimation of the fluoroscopic intrinsic parameters.

3.3.2 Error Incurred From Perspective Projection Distortion

To quantify the distortion attributed to magnification and perspective projection the segmented centroids of the 3D grid phantom were registered to a point cloud representing ideal locations for the BBs in the phantom. Registration of the two point clouds was performed using images captured from a flat panel and image intensifier system. In order to determine how closely fluoroscopic images follow a projective camera model, centroids were also transformed to the camera coordinate system using the calculated intrinsic parameters of the fluoroscope. The single directional RMS and total RMS error between actual and registered points was recorded for each point cloud.

3.3.3 Error Incurred from Fluoroscopic Image Distortion

A 10 cm x 10 cm checkerboard phantom with markers at 1 cm isotropic intervals was constructed to quantify the distortion from the fluoroscope. The phantom

was composed of acrylic due to its radiolucency, with a series of targets etched using a laser milling machine. Each target point was enhanced using radiopaque media, thus causing high contrast between the target points and the background.

The checkerboard phantom was traversed through the fluoroscopic volume at 2 cm intervals over a total range of 54 cm along the direction of the x-ray beam. At each interval point, a single fluoroscopic frame was acquired. Each image was 9 x 9 median filtered and color inverted prior to processing to reduce false vertex detection due to random shot noise. Gray-level threshold selection was performed using Otsu‘s method whereby a binary mask image was then created [48]. The connected components algorithm was used to detect individual markers in the frame allowing for quantization of vertex count and assignment of points allowing detection in subsequent frames invariant of translation and scale. To provide further consistency across frames and lessen the impact of incomplete marker detection, the gray weighted centroid for each vertex was calculated. Centroid alignment through the fluoroscopic volume was achieved through the co-registration of the images using a point-based rigid Procrustes approach.

From this volume, a scatter field was created to visualize the distortionary effects. Lines were drawn between the points of the center frame of the volume to visualize the extent of distortion. Centroid position was plotted along the z-axis and a line was fit to each of the corresponding points in each frame to determine the level of projection through the volume.

This method was repeated for both a traditional image intensifier (II) based fluoroscope, and flat-panel or solid-state fluoroscope.

3.3.4 Case Study Testing Projective Transform Error

Perspective projection error using camera points transformed from image points was tested using a cardiac phantom model. Design of the cardiac model consisted of two plastic boxes with tubing used to represent vasculature (Figure 3.3). The first of the boxes represents the chest cavity and is 200 mm x 200 mm x 96 mm made from 3 mm thick acrylic. A smaller box was used to represent the heart and has dimensions of 104 mm x 75 mm x 70 mm. Fluoroscopic images of the phantoms were captured in the AP and lateral planes and a registration between the images and the magnetic tracker was performed. Transformed points were overlaid onto the images to visualize the inaccuracy of the registration and the amount of error that still exists.

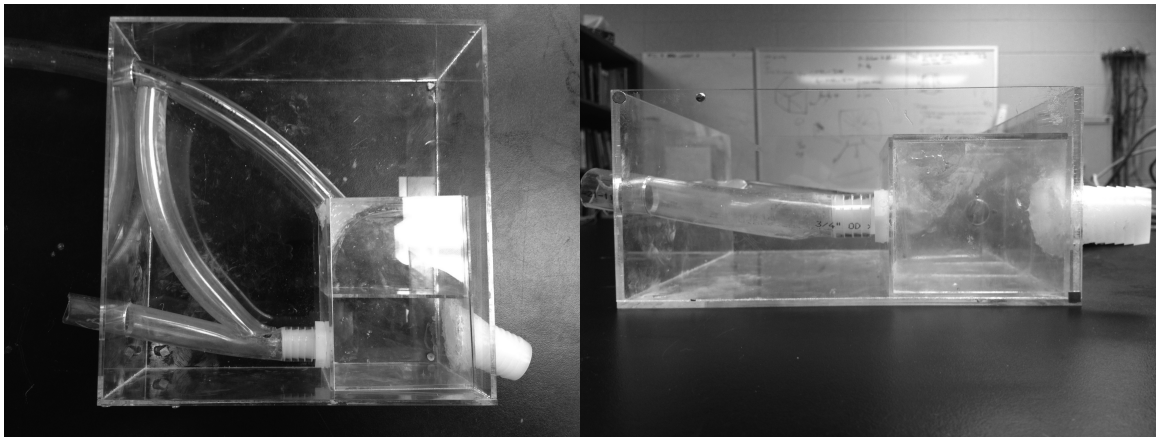

(a) (b)

Figure 3.3: Cardiac phantom used to assess the correction method presented. (a) Top-view. (b) Side-view.

3.4 Results and Discussion

Image guided procedures require accurate reporting of tool locations and structural locations through medical images. Image-to physical space registration provides

a mapping between physical space and image space. Fluoroscopy offers real time capture of anatomy but image intensifiers introduce too much error into the images to be a completely viable solution. When bi-plane fluoroscopic systems are utilized the correction between the two images will need to vary as each II is inherently different due to the manufacturing process. Flat panel fluoroscopic systems, although more expensive, offer greater spatial resolution without the pincushion and 'S' distortion found in II systems [12]. Flat panel systems continue to have perspective projection distortion, which is a function of the x-ray beam geometry.

3.4.1 Automated Estimation of Fluoroscopic Intrinsic Parameters

	AP Flat Panel	Lateral Flat Panel	Image intensifier
u_0	255.7092	279.2698	209.6545
v_0	372.362	403.9742	327.9788
f	383.0563	755.8195	1.04E+03

Table 3.1: Calculated intrinsic parameters for the lateral and AP plane of the flat panel and image intensifier fluoroscope.

Evaluation of the perspective projection distortion in fluoroscopy required the use of the intrinsic parameters which are calculated during calibration. Our automated method for calibration of the fluoroscope was tested on a flat panel bi-plane system and an II c-arm system. Values for each intrinsic parameter were calculated using a single image frame of the 3D grid phantom facing the x-ray source (Table 3.1). It has been shown that intrinsic parameters calculated during calibration can vary dependent upon the orientation of the c-arm fluoroscope resulting in a mean projection error of 0.63 mm for image intensifier systems [57]. This orientation error is negligible for this study as the orientation of the fluoroscope was maintained for

collection of the error analysis images and the calibration images. Another reason for not considering orientation error is that no evidence has been presented that shows flat panel systems experience this error.

3.4.2 Error Incurred From Perspective Projection Distortion

Figure 3.4 shows the error between the point clouds for all three representations of the phantom. Transformed points (triangles) from the registration are overlaid onto a grid representing ideal locations (cross) where any offset between the two markers signifies error. Error between the real world representation, the image representation and the camera representation of the 3D grid phantom was explored. It is clear from the plots that the camera point cloud has a better fit than the image point cloud. We attribute the better fit to the transformation of the image point cloud to the camera point cloud using the calculated intrinsic parameters. Although the fit is better for the camera point cloud, there is still error apparent in the fit between the two point clouds. RMS distance error between points in each axis is given in Table 3.2.

	Error (X)	Error (Y)	Error (Z)	Total Error (X, Y, Z)
FP - Lateral - WC	0.80	0.93	0.83	1.49
FP - Lateral - WI	0.31	0.98	10.90	10.95
FP - AP - WC	1.47	1.34	2.39	3.11
FP - AP - WI	0.40	0.48	10.90	10.92
II - WC	1.94	1.27	5.25	5.74
II - WI	0.43	0.87	8.23	8.28

Table 3.2: RMS error for registration between world, camera, and image point clouds in millimeters for each direction and total directional error. WC is world to camera and WI is world to image.

Error between the fit for the point clouds displayed in Table 3.2 revealed that there was more error in the fit between the image and world point cloud than the

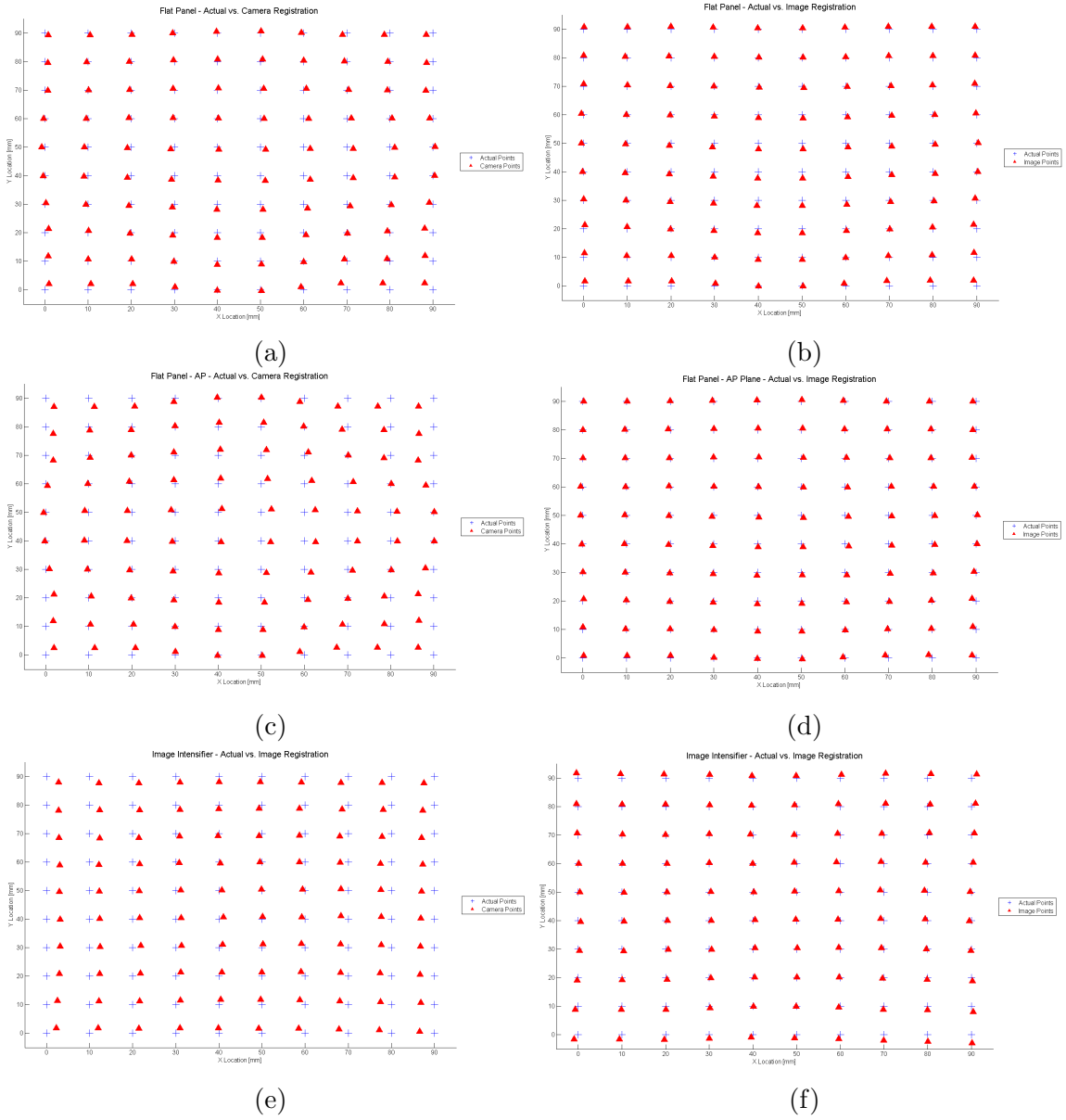

Figure 3.4: Centroid grids of the 3D grid phantom where the transformed camera point cloud was registered to the world point cloud (a,c,e) and the image point cloud was registered to the world point cloud (b,d,f).

camera and world point cloud. RMS distance error in the z direction decreased following the transformation into camera coordinates whereas error in the x and y directions increased for the same transformation. We believe this decrease in error in the z direction is attributed to the removal of projective distortion during the camera

space transformation. It was also observed that there was higher error in the II image point cloud even after the camera space transformation. This high residual error is likely due to the pincushion and 'S' distortion in the image. Error values for the fluoroscope images are non-issue for some IGS studies but can mean missing a target in high precision procedures where 1 mm of error can mean failure.

3.4.3 Error Incurred from Fluoroscopic Image Distortion

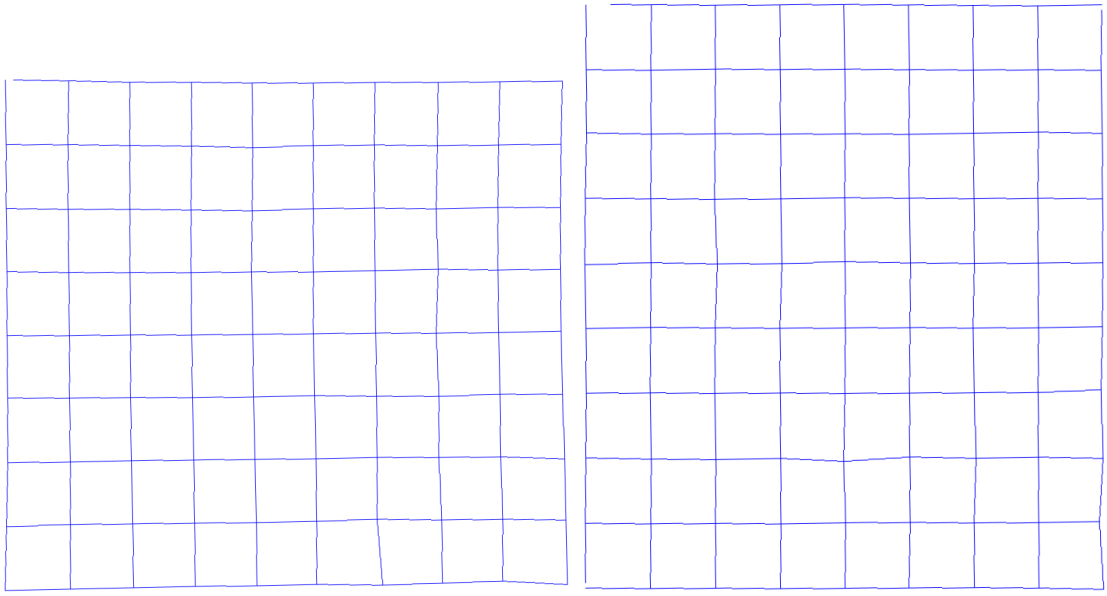

(a) (b)

Figure 3.5: Single frame with markers connected to each neighbor to form a grid. (a) Constructed using images from the II, pincushion distortion is grossly apparent and there is slight 'S' distortion. (b) Grid from solid state detector, lines are straight and there appears to be little to no distortion.

A line was drawn between the centroids in the center frame of both fluoroscopic image sets to determine the presence and extent of pincushion distortion. The centroid grid from the II in Figure 3.5 shows clear signs of pincushion distortion along the edges and there is slight 'S' distortion along the vertical axis of the image. Full contribution

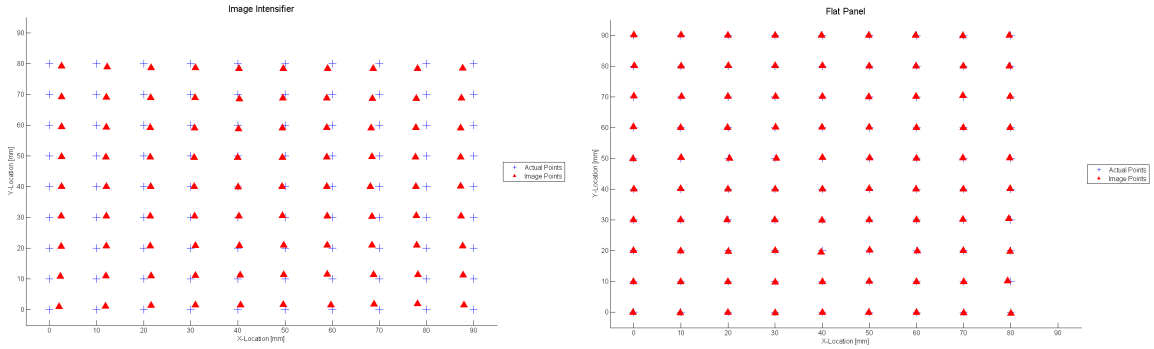

(a) (b)

Figure 3.6: Centroid grids of a single frame from the 2D grid phantom volume traversal through a flat panel and image intensifier fluoroscope. (a) The error appears to be high as many of the image points don't map well to world points which is expect for image intensifier systems due to pincushion and 'S' distortion. (b) Transformed camera points have a good fit with the world point cloud and the amount of error is significantly lower.

of these errors was not characterized but has been previously studied [72]. Deviation from world coordinates for the 2D centroid grids was investigated and the centroid plots for the II and flat panel fluoroscopes are shown in Figure 3.6.

	RMS Error (X)	RMS Error (Y)	RMS Distance Error (X, Y)
Image Intensifier	1.65	11.83	11.94
Flat Panel	0.12	0.13	0.18

Table 3.3: Average directional error values in millimeters for a single frame of the 2D centroid grid fluoroscope volume capture in millimeters. Error for the image intensifier fluoroscope is significantly higher than the flat panel fluoroscope.

The flat panel fluoroscope appears to have a better fit to the world coordinates than the II fluoroscope. RMS distance error for each point along the x and y directions as well as the total distance error for each fluoroscope can be found in Table 3.3. Error for the flat panel fluoroscope is significantly lower than the II fluoroscope. This shows that flat panel fluoroscopes have very low rates of error when capturing objects on a single plane but with the addition of the z-plane the error increases to greater than

1 mm.

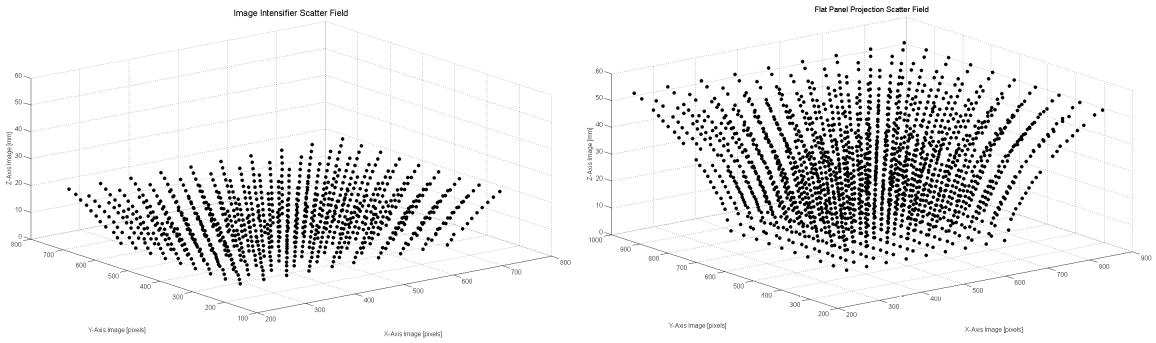

(a) (b)

Figure 3.7: Scatter fields of the centroids from each marker as it was traversed through the imaging volume of the image intensifer 3.7a and flat panel 3.7b fluoroscopes.

Perspective distortion and magnification can be clearly visualized in the scatter field plots of Figure 3.7 where a scaling factor was not used in the registration. As the distance from the source increased, the locations of the centroids converged towards the center of the image. The scatter field plot for the II does not cover the same depth as the flat panel system because magnification in the images prevented centroids from being captured. Each scatter field plot reveals the inherent nature of the fluoroscopic imaging system. A single point can be shifted by hundreds of pixels just by adjusting the depth of the point. Points on the same line in the z direction will no longer appear as such in resultant images and this is a cause of error in reported point locations.

3.4.4 Case Study Testing Projective Transform Error

The effect of perspective projective distortion in fluoroscopic images is clearly seen by the results of registration with a tracking system shown in Table 3.4. The registration using the image point cloud yielded a transformation with a high RMS total distance error value between the input and transformed points. Error values from the registered cardiac phantom dataset show that a viable registration between

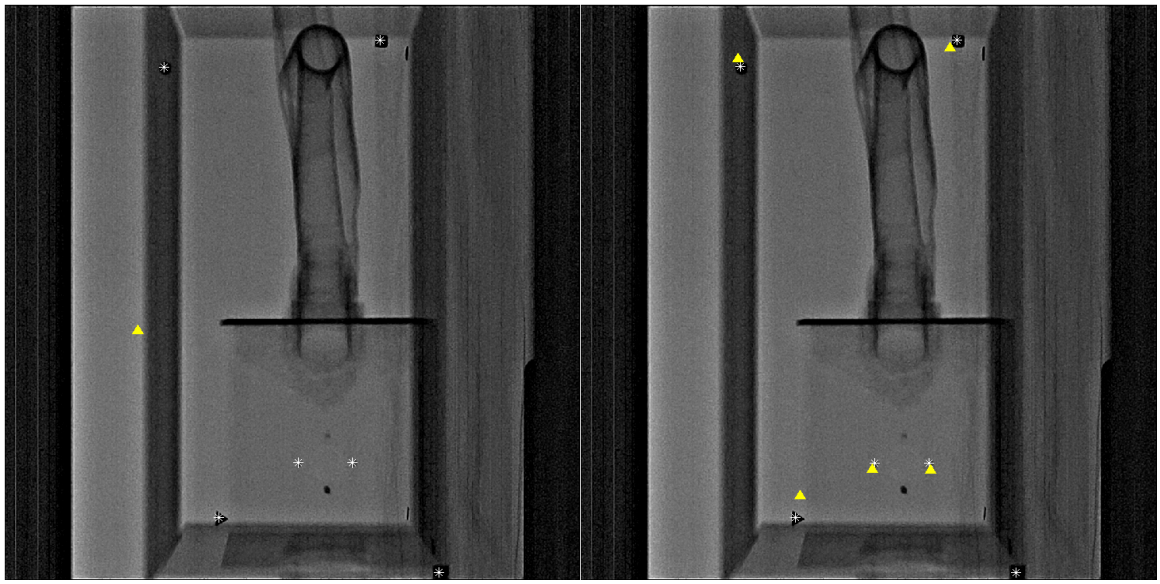

(a) (b)

Figure 3.8: Cardiac phantom case study images where the triangles are the transformed tracker points and the stars are the target points. (a) Image points without camera space transformation used for registration. (b) Camera space points used in calculation of registration matrix.

	Error (X)	Error (Y)	Error (Z)	RMS Distance Error (X, Y, Z)
Image	115.765	114.906	4.416	163.170
Camera	2.057	4.307	0.572	4.808

Table 3.4: RMS error values in millimeters for the registration between image points and collected tracker points as well as transformed camera points and collected tracker points. The camera coordinates produced a significantly better fit than the image points which means points should be transformed into the camera coordinate space prior to being used in a registration.

the images and tracker space could not be achieved using image cloud points alone. Registration using the camera point cloud yielded better results but still returned error values that were relatively high for points located at the boundary of the image. Even with such levels of error, the registration was accurate enough to allow for guidance of tracked catheters through obstacles in the phantom. A projective registration will be used in future studies involving fluoroscopic images while further work will be

done to increase the level of accuracy obtained from the registration.

3.5 Conclusion

Characterization of the fluoroscope is essential in calculating a transformation matrix that leads to low error in transformed points. The results show that the modern flat panel fluoroscope produces images free from image capture distortion but still require compensation for the projective nature of the images. Images from image intensifier fluoroscopes need to have correction for pin cushion and S distortion applied prior to being used in an image-guided setting. Image-guided procedures have shown to be an effective means of reducing patient trauma and when coupled with fluoroscopy it will reduce radiation exposure to clinicians and patients. Through this work we characterized the fluoroscope by investigating the intrinsic properties of the system focusing on introduction of error and level of hindrance the projective nature of the images have on IGS applications.

Chapter 4

Efficacy of a Novel IGS System in Atrial Septal Defect Repair

4.1 Abstract

Congenital heart disease occurs in 107.6 out of 10,000 live births, with Atrial Septal Defects (ASD) accounting for 10% of these conditions. Historically, ASDs were treated with open heart surgery using cardiopulmonary bypass, allowing a patch to be sewn over the defect. In 1976, King et al. demonstrated use of a transcatheter occlusion procedure, thus reducing the invasiveness of ASD repair. Localization during these catheter based procedures traditionally has relied on bi-plane fluoroscopy; more recently trans-esophageal echocardiography (TEE) and intra-cardiac echocardiography (ICE) have been used to navigate these procedures. Although there is a high success rate using the transcatheter occlusion procedure, fluoroscopy poses radiation dose risk to both patient and clinician. The impact of this dose to the patients is important as many of those undergoing this procedure are children, who have an increased risk associated with radiation exposure. Their longer life expectancy than

adults provides a larger window of opportunity for expressing the damaging effects of ionizing radiation. In addition, epidemiologic studies of exposed populations have demonstrated that children are considerably more sensitive to the carcinogenic effects radiation.

Image-guided surgery (IGS) uses pre-operative and intra-operative images to guide surgery or an interventional procedure. Central to every IGS system is a software application capable of processing and displaying patient images, registration between multiple coordinate systems, and interfacing with a tool tracking system. We have developed a novel image-guided surgery framework called Kit for Navigation by Image Focused Exploration (KNIFE). In this work we assess the efficacy of this image-guided navigation system for ASD repair using a series of mock clinical experiments designed to simulate ASD repair device deployment.

4.2 Introduction

An ASD is classified based on its anatomical location with the main types being, ostium secundum, ostium primum, and sinus venosus. Multiple types of ASDs exist with classification based upon anatomical location on the septal wall; the most prevalent and easiest to repair of these is the ostium secundum. Historically, ASD treatment has involved open-heart surgery where smaller defects are primarily sutured closed and larger defects are patched using a variety of surgical materials. Transcatheter occlusion has become the gold standard for ASD repair, minimizing the need for more invasive procedures such as surgery, which is now reserved for defects which are not amenable to device closure [20]. As catheter interventions do not allow for direct vision of internal anatomy medical imaging is used for navigation of therapy. Traditionally bi-plane fluoroscopy has been used for this navigation. Flu-

oroscopy however poses risk to both the patient and the clinician due to radiation exposure. Trans-esophageal echocardiogram (TEE) and intra-cardiac echocardiography (ICE) have been recently introduced to decrease the use of fluoroscopy. Clinical studies have also shown successful closure of ASDs using only ultrasound techniques in limited cases [62]. Transcatheter occlusion procedures offer an improvement to invasive surgery though the patient and clinician are subjected to exposure of ionizing radiation.

In recent years, government agencies and research institutions have been publishing work that investigates the risk that ionizing radiation from diagnostic tools poses to patients [69, 56, 54]. A study done on clinicians, to evaluate the relationship between working in a cardiac catheterization laboratory and cancer risk showed that interventional cardiologists had the highest levels of exposure amongst other medical users of x-rays. It was also found that over the professional lifetime (11-26 years) of catheterization laboratory workers, median lifetime attributable risk of fatal cancer was 1 in 384 and 1 in 192 for fatal and nonfatal cancer [69]. Since effective dosage is cumulative over lifetime, the longer an interventional cardiologist practices, the higher the risk they will have of developing cancer.

Patient cumulative dose in interventional cardiology procedures has also been studied. A study looking at these occlusion procedures found the mean time for fluoroscopic use was 20.7 ± 12.8 minutes over an average procedure time of 105.7 ± 43.2 minutes. This fluoroscopic time accounted for approximately 20% of the total procedure time [20]. Over the course of the procedure, effective radiation dosages have been shown to be 3.5-8.0 mSv with an average of 5.3 mSv [20]. A brain CT study has dose ranging from 0.8-5 mSv and a chest CT with dose ranging from 6-18 mSv [20]. Currently, there is a growing awareness over the long term effects of radiological procedures [25]. In a study involving monitoring cumulative patient lifetime

effective dose in cardiology, arteriography and interventional procedures accounted for approximately 48% of the average dose per patient [10]. This equates to roughly 30 mSv, where the international commission on radiological protection (ICRP) has approximated the additional lifetime risk of fatal cancer to be 1 in 20,000 per mSv [1].

A second study found that a large percentage of radiological examinations were related to interventional cardiology [10]. In recent years, the use of medical radiation in interventional cardiology procedures has increased so much it is becoming a public health issue [24]. Results showed that over patient lifetime, the median cumulative dose was 61 mSv with the range being 3-441 mSv [10]. Interventional cardiology was attributed with 48% of the cumulative dose of patients while only accounting for 12% of total procedures over patient lifetime. Reduction of exposure is critical for cardiology patients as their cumulative exposure levels put them at a 1 in 200 risk of cancer. Image-guided procedures can reduce the exposure of patients and clinicians without drastically changing current interventional cardiology techniques.

Image-guided surgery (IGS) systems allow for the visualization of subsurface tissues and structures not otherwise visible. These systems use pre-operative and intra-operative images as a representation of the physical patient. Images are co-registered with a tracked tool within the procedure room. The location of these tools is displayed in the context of the radiological images. Presently, there are a number of both commercial and research systems available, all based on the general scheme mapping tracked tools back to a set of pre-operative or intra-operative images. For example, from industry Medtronic produces StealthStation, from academia Vanderbilt University has ORION, and the open-source community via Kitware produces IGSTK [65, 28]. Other notable systems include Mayo Clinic's FINDER and open source 3D Slicer based on the NA-MIC kit [60, 29] Each of these systems has both

benefits and drawbacks based on their design and implementation, making no solution ideally suited to perform these transcatheter procedures. The StealthStation is primarily designed for neurosurgery, and is based on a proprietary code base, thus complicating the ability to do novel cardiac research. ORION is unable to directly import DICOM images, but does have the ability to capture real time image feeds from a fluoroscope through a frame grabber. IGSTK is not a standalone application but rather a framework for development of novel applications, this framework however does not completely satisfy procedural requirements for ASD repair. Through examination of these systems we have undertaken the development of a novel system, the Kit for Navigation by Image Focused Exploration (KNIFE).

4.3 Methods

Evaluation of the efficacy of the KNIFE IGS system was performed by constructing a series of cardiac phantoms, each of which mimicked an ASD. These phantoms were designed using CAD software and then laser cut from clear acrylic sheets. Each phantom was designed to have two chambers that represented the atria, with a defect ranging from 15 – 20 mm on the separating wall (Figure 4.1). Three inlet holes were cut into each phantom, representing the inferior and superior vena cava as well as the pulmonary vein.

Each cardiac phantom was then placed into a secondary chest cavity phantom with tubing connecting the various portals mimicking the surrounding vasculature. Configuration of the tubing varied to provide different levels of difficulty in the mock procedures. Each chest cavity phantom was designed so as to have multiple checkpoints where the current procedure time would be recorded. A BB was placed iIn each corner of the chest cavity to serve as a fiducial for a rigid and projective based

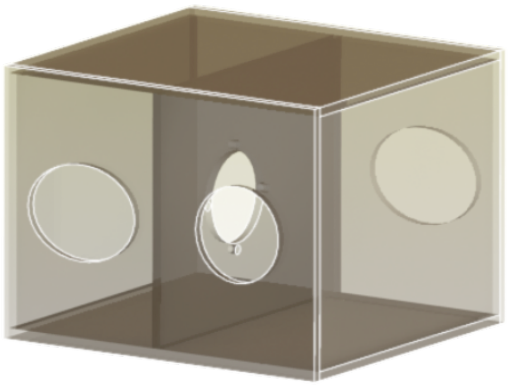

Figure 4.1: CAD rendering of cardiac phantom model where transparency was used to visualize the internal defect in the chamber wall

registration algorithm.

To validate our system a clinician, who specializes in congenital defect repair, drove a catheter through a phantom model using our IGS system and then with traditional bi-plane fluoroscopic techniques. A two second bi-plane fluoroscopic loop was collected using a flat panel fluoroscope (Toshiba Inc., tawara-shi, Tochigi-ken, Japan) then exported and loaded into KNIFE (Figure 4.2). A projection based Procrustes registration was performed to obtain a transform between the fluoroscopic loop and the tracking system. We localized the catheter position using an Aurora (Northern Digital Instruments, Waterloo, ON, Canada) magnetic tracker with a 6 degree of freedom flex cord sensor embedded within a 7 fr. angio-catheter. Catheter tip position reported from the tracker, was overlaid onto the bi-plane loop while the clinician drove the catheter through the phantom. Two studies were performed using these methods.

The first of these studies involved measuring the time taken to traverse the defect, then exit out of the superior vena cava followed by going back across the defect and out the pulmonary vein. The time at each point was recorded for a total of 40 trials using either the IGS system or the traditional fluoroscopic technique. A

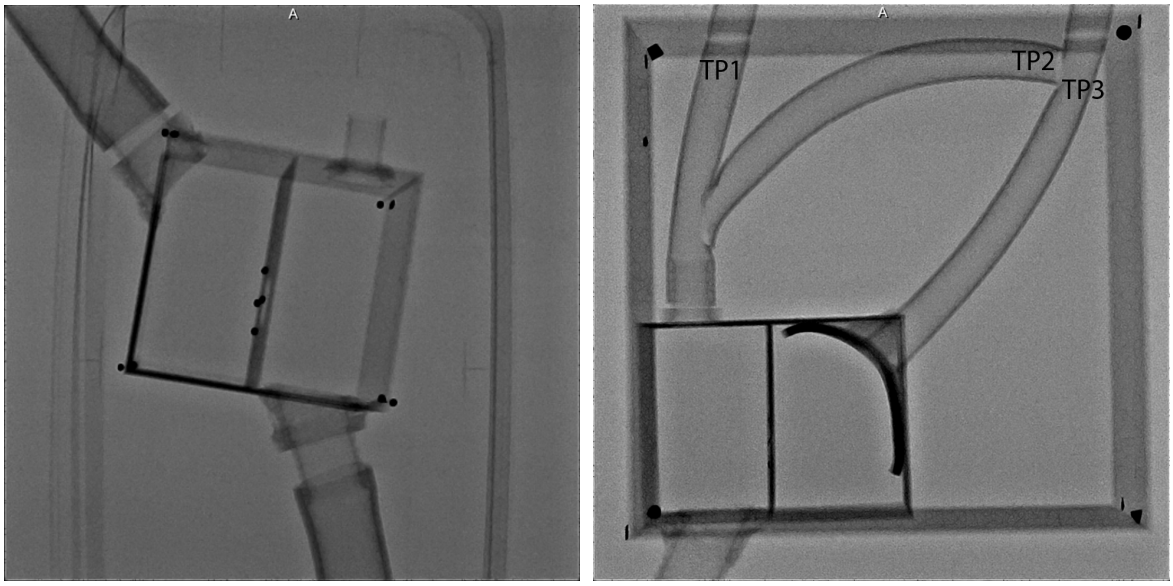

(a) (b)

Figure 4.2: (a) Fluoroscopic frame of cardiac phantom only (b) Fluoroscopic frame of cardiac phantom embedded in the chest cavity phantom where tubing simulates vasculature.

two mean t-test was conducted using the collected data at each of the separate time points.

Three time checkpoints were established in the chest cavity phantoms and a mapping of the points can be found in Figure 4.2b. Each time point was recorded for both the IGS system and the bi-plane fluoroscope. Radiation dosage was measured using a Bleeper mR (Vertec Scientific Ltd., Reading, UK) during the collection of the fluoroscopic cine loop to be used in the IGS system as well as during each of the trials where the fluoroscope was used for guidance. The radiation dosage experienced by the clinician was also measured.

4.4 Results

In the cardiac phantom study, time to reach the ASD, the superior vena cava and the total procedure times for the first phantom over the 40 trials are shown in Figure 4.3a. Mean total procedure time for bi-plane fluoroscopy guidance was 25.70 seconds, while for KNIFE the mean time was 21.76 seconds. A one-tailed t-test showed a significant difference in the procedure times for the two guidance techniques ($p < 0.05$). Time to reach the pulmonary vein (PV) using bi-plane fluoroscopy was not recorded and is absent from the results. Average procedure times for the chest cavity phantom were 17.55 seconds and 32.71 seconds for bi-plane fluoroscopy and KNIFE respectively. Average dosage for fluoroscopy guided procedures vs. KNIFE guidance is shown in Figure 6.2.

4.5 Discussion and Conclusions

Use of an IGS system in ASD repair allows for less use of ionizing radiation, significantly lowering the absorbed dose of the patient and clinician. As radiation dose is cumulative over lifetime, the more procedures that patients undergo and clinicians perform, the greater their likelihood of developing both fatal and non-fatal cancer. In recent years, interventional cardiology procedures have seen immense growth with an increase of 264% in the number of coronary angiographies alone [56]. Advancements in imaging technology has driven such growth in procedure count but there has been a general disregard for the negative health implications such technology carries. IGS systems in interventional procedures offer a tradeoff between real time images and absorbed dose while still permitting use of current techniques.

Procedure times for the simple cardiac phantom using KNIFE were signifi-

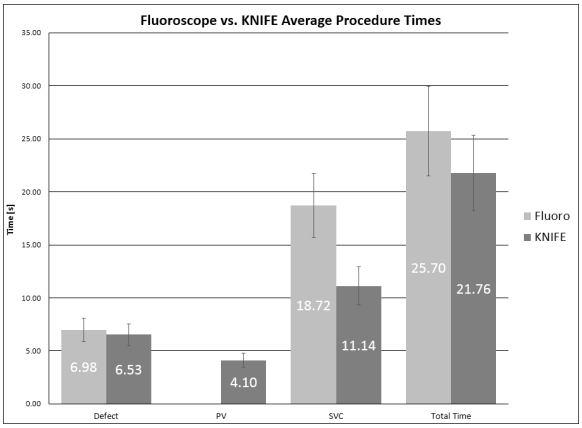

(a)

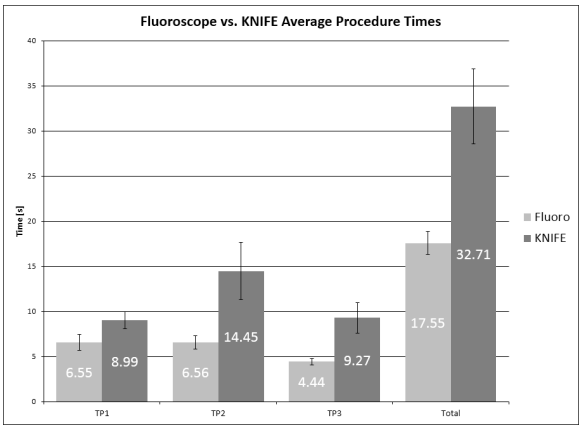

(b)

Figure 4.3: Average procedure times at various check points. (a) Cardiac phantom only timings, no data for fluoroscopy time at PV is available. (b) Cardiac phantom + chest cavity timings.

cantly faster than fluoroscopy guidance alone ($p < 0.05$) (Figure 4.3a). Times for KNIFE were faster at more complex locations within the cardiac phantom due to real time position update. Fluoroscopy guidance required the clinician to switch between AP and lateral imaging planes in order to position the catheter properly with any movement invalidating previously collected images. The lack of positional data that is consistent in both imaging planes makes fluoroscopic guidance difficult for non-expert users and clinicians alike. Chest cavity and vascular system phantom timings were significantly lower for fluoroscopy guidance ($p < 0.05$) (Figure 4.3b).

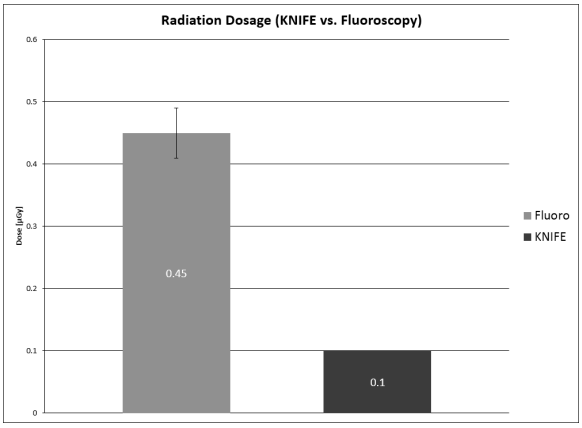

Figure 4.4: Average absorbed dose for both guidance techniques. KNIFE dosage levels are from the initial fluoroscopic cine loop collection.

These timings are likely lower due to the increase in complexity of the phantom and the lack of catheter shape information in KNIFE. Knowledge of catheter tip direction and catheter shape during fluoroscopy guidance allows the clinician to make informed decisions about how they will move the catheter to reach the time check points.

Absorbed dose data from this initial study showed that the KNIFE IGS systems has significantly less radiation exposure when compared to fluoroscopy. As fluoroscopic procedure times increase, patient and clinician absorbed dose will also increase while in KNIFE the dosage only increases with each newly acquired cine loop. Average fluoroscopy time for transcatheter ASD repair was 17.6 minutes ranging from 5.2 to 41.2 minutes [75]. Fluoroscopy use during the chest cavity and vascular system phantom was on average 17.55 seconds with an average patient absorbed dose of 0.45 μGy. By extrapolating this absorbed dosage, over the average 17.6 minutes, these fluoroscopic procedures will result in around 27 μGy while KNIFE would remain relatively constant, only dependent upon the number of cine loops collected.

Transcatheter ASD repair is typically performed using fluoroscopy guidance but the effects of radiation exposure on the patients and clinicians has raised con-

cerns. Ultrasound has been utilized to supplement fluoroscopy but has limitations such as poor catheter and device visualization when not viewing the immediate area. Furthermore, the catheter cannot be visualized outside of the heart using ultrasound leading to clinicians only using it when fluoroscopy is contraindicated for the patient. KNIFE guidance allows for minimization of exposure levels while permitting visualization of the catheter tip localized within the captured fluoroscopic cine loop. Further improvement of the KNIFE IGS system has the potential to reduce radiation exposure levels in ASD repair and other interventional cardiology procedures.

Chapter 5

Heuristic Estimation of Electromagnetically Tracked Catheter Shape for Image-Guided Vascular Procedures

5.1 Abstract

In our previous work we presented a novel image-guided surgery (IGS) system, Kit for Navigation by Image Focused Exploration (KNIFE) [38, 43]. KNIFE has been demonstrated to be effective in guiding mock clinical procedures with the tip of an electromagnetically tracked catheter overlaid onto a pre-captured bi-plane fluoroscopic loop. Representation of the catheter in KNIFE differs greatly from what is captured by the fluoroscope, due to distortions and other properties of fluoroscopic images. When imaged by a fluoroscope, catheters can be visualized due to the inclusion of radiopaque materials (i.e. Bi, Ba, W) in the polymer blend [16]. However,

in KNIFE catheter location is determined using a single tracking seed located in the catheter tip that is represented as a single point overlaid on pre-captured fluoroscopic images.

To bridge the gap in catheter representation between KNIFE and traditional methods we constructed a catheter with five tracking seeds positioned along the distal 70 mm of the catheter. We have currently investigated the use of four spline interpolation methods for estimation of true catheter shape and have assesed the error in their estimation of true catheter shape. In this work we present a method for the evaluation of interpolation algorithms with respect to catheter shape determination.

5.2 Introduction

Congenital heart disease (CHD) occurs in approximately 8 in 1000 live births [10]. Recently, incidence rates of children with CHDs has driven a legislative push in South Carolina resulting in a new law requiring newborns to be screened for congenital heart diseases within 72 hours after birth [3]. Over the years, concerns over children born with a congenital heart defect has increased greatly due to the treatable nature of a disease that often goes undiagnosed.

The current standard of care for children born with a congenital heart disease (CHD) is the delivery of a catheter equipped with an occluder mesh device or an embolization coil to the defect location whereby the tool is deployed or activated. While minimally invasive catheter procedures are less traumatic than open heart surgery, numerous studies have shown interventional cardiology to be the largest medical user of ionizing radiation [40, 34, 49]. High usage of ionizing radiation amongst interventional cardiologists stems from a reliance on fluoroscopy for guidance of tools such as the catheter. Clinicians often collect several cine loops (short videos) and use an

average 20.7±12.8 minutes of fluoroscopy while guiding a catheter since new images must be captured to visualize any changes in catheter position or orientation [20]. Additionally, bi-plane systems are updated asynchronously allowing visualization in only a single plane at a time which requires extensive training to become adequately skilled [26].

Radiation exposure to interventional cardiology patients carries significantly higher risk as they are in the direct path of the x-ray beam. A cumulative patient dose study across cardiology found that interventional and nuclear medicine procedures accounted for the highest levels of exposure per procedure [7]. Age and gender also affect lifetime attributable risk as a 64-slice CT in a 20 year old woman would result in a 1 in 140 risk but would only be 1 in 5000 for an 80 year old man.

Children being treated for congenital heart disease (CHD) are especially vulnerable. Many therapeutic interventions for CHD patients have transitioned from open surgical procedures to minimally invasive, catheter-based procedures requiring fluoroscopic guidance. While this trend has many benefits, it unfortunately results in excessive cumulative radiation exposure to children who often must undergo multiple, complex catheter procedures. Moreover, recent studies in children with CHD who have undergone catheterization have demonstrated direct DNA evidence of long-lasting chromosomal damage [9, 7]. This alarming evidence underscores the need for an alternative to ionizing radiation to guide cardiac catheterizations in children.

Work on simulation of guide-wire and catheter shape for use in virtual procedures has produced complex models for estimating catheter shape [36]. These models are based on analytical methods that while simple to calculate require knowledge of the anatomy in the scene which is excessive to calculate in an IGS procedure where partial tool locations are known. In a literature review of catheter shape estimation it was found that little work had been done regarding estimation of shape from tracked

regions in the context of fluoroscopy driven vascular procedures. Dore, et al successfully used the methods mentioned in Konings' work along with EM tracked seeds to estimate catheter shape in a CT guided robotic catheterization procedure [19, 36].

While such complex models are useful in simulation and robot assisted catheter navigation studies they are unusable for clinician controlled image-guided vascular procedures reliant on preoperative and intraoperative fluoroscopic images. Fluoroscopy captures a 2D representation of the anatomy unlike CT and MRI which are 3D imaging modalities. Additionally, fluoroscopic images capture a perspective representation where objects further from the x-ray source appear smaller. This geometric distortion requires camera calibration of the fluoroscope before images can be used in the 2D-3D registrations of IGS systems.

In our previous work we explored the application of image-guided surgery (IGS) techniques to interventions for repair of atrial septal defects, a type of congenital heart defect. Our IGS software system, Kit for Navigation by Image Focused Exploration (KNIFE), was able to facilitate guidance of a catheter with an electromagnetically tracked 6 degrees of freedom seed at its tip in phantom trials. While KNIFE guidance led to a reduction in radiation exposure, lack of full catheter shape during trials made procedures more difficult leading to longer trial times.

The purpose of this paper is to measure the error in spline representation of electromagnetically tracked catheters in image-guided vascular procedures. We will assess the estimation of shape error for four interpolation algorithms with the intent of determining which algorithm is best suited for use in image-guided vascular procedures where the full shape of the catheter must be presented to the clinician.

5.3 Methods

KNIFE was compared in our previous work to traditional fluoroscopic techniques in which a catheter was guided to predetermined points in a cardiac phantom. In fluoroscopic images, a partial shadow of the full shape of the catheter can be visualized as the material is intended to be radiopaque. During KNIFE guidance however, only the tip of the catheter was recorded using an Aurora electromagnetic tracker (Northern Digital Instruments, Waterloo, ON, Canada) and subsequently was rendered on pre captured images. In our initial study we found that KNIFE led to faster procedure times but a follow up study found different results likely due to an increase in difficulty in the mock procedure. The follow up study also recorded data regarding absorbed dose, showing that KNIFE led to a significant ($p < 0.05$) decrease in the absorbed dose over the course of the mock procedure.

5.3.1 Construction of EM Tracked Shape Catheter

We have developed a magnetically tracked catheter with five 5DOF sensors placed at varied locations along the inner lumen of a 7F catheter. Seed placement was determined by which region of the catheter would be visible during interventional cardiac procedures once the catheter has reached the patients heart. The two most distal seeds are placed closer to provide greater shape estimation accuracy near the catheter tip as false location reporting at the tip could result in incorrent catheter navigation. Verification of seed placement was accomplished by capturing a planar x-ray image of the constructed catheter.

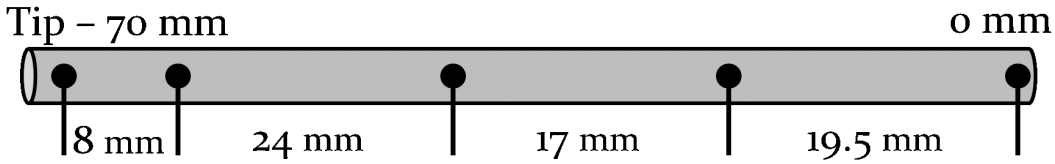

Figure 5.1: Graphical representation of the designed EM tracked shape catheter. Tracking seeds are positioned to maximize tracking accuracy in the region of the catheter most commonly used during interventional procedures where only a small portion of the catheter is visible at any time.

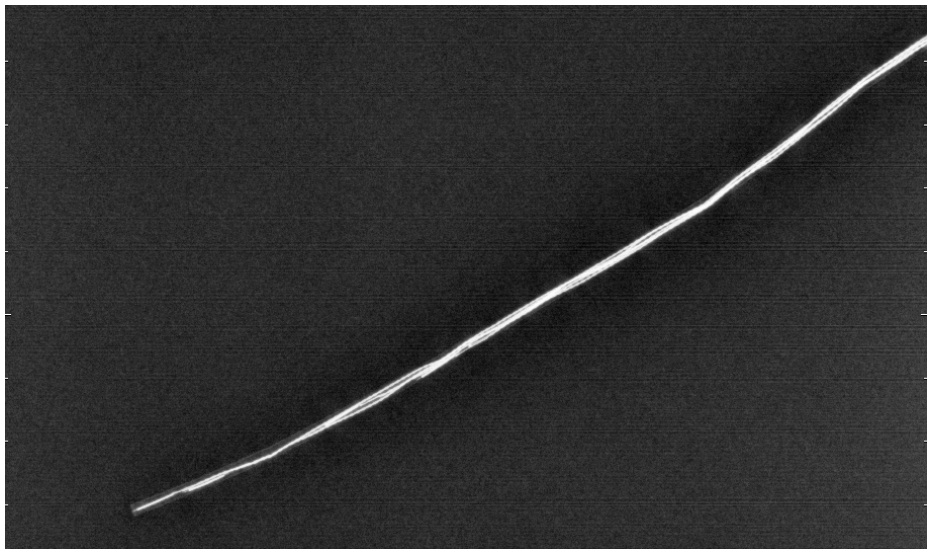

Figure 5.2: Planar x-ray of shape catheter used for verification of seed placement along the catheter's inner lumen.

5.3.2 Estimation of True Catheter Shape using Reported Seed Locations and Orientations

Position and orientation of each tracking seed in the catheter can be defined as $x_i = (x, y, z, \alpha, \beta, \gamma)$, where (x, y, z) is the spatial position and (α, β, γ) is the orientation in each direction of the seed relative to the trackers coordinate system. In order to represent the shape of the catheter in pre-acquired images a spline must

connect each neighboring known point. While there are a wide plethora of interpolation algorithms available, we chose to use four interpolation methods. Each algorithm was tested for their accuracy and conservativeness when estimating shape between known point locations. The interpolation algorithms evaluated were linear, cubic spline, shape preserving piecewise cubic spline, and cubic hermite spline with tangents based on reported seed orientations.

In order to evaluate each interpolation algorithm we constructed a controlled path from CAD designed and laser cut stacked 2 mm acrylic sheets. A tube was then embedded along the cut path to provide a lumen for the catheter to traverse. The controlled path was designed to provide multiple poses of the shape catheter allowing for a more complete analysis of how each interpolation algorithm estimates true catheter shape. Images of multiple catheter poses were captured using a camera mounted to a tripod position above the designed path. For each image of the catheter pose, tracker seed locations and orientations were captured to use in estimating true shape. Mapping of the EM tracker coordinate system to the image coordinate system was accomplished prior to any error assessment using a rigid registration. Initial segmentation of the catheter in captured images was accomplished using simple thresholding based on 10% of the maximum value pixel value of the catheter. Midline of the catheter was attained using the midpoint of the boundary edges generated from canny-edge detection on the thresheld image.

Shape estimation error can be calculated using the Hausdorff distance between the interpolated curve and the generated midpoint curve from the captured images. The Hausdorff distance allows for the measurement of distance between two point subsets based on the distances between each point in each subset. Mathmatically, the Hausdorff distance is defined as:

$$d_{\mathrm{H}}(X,Y) = \max\{\, \sup_{x\in X} \inf_{y\in Y} d(x,y),\, \sup_{y\in Y} \inf_{x\in X} d(x,y) \,\},$$

where point subset X includes the interpolated spline points while point subset Y is the collection of cather midpoints. A secondary measure of estimation error used is the difference between the interpolated segment lengths l_i and the known actual lengths L_i. Error in estimated segment lengths allows for determination of how conservative the algorithm in interpolating the unknown points in a segment. Measurement of how conservative an interpolation algorithm is important in scenarios where there is little margin for representation of false data.

5.4 Results

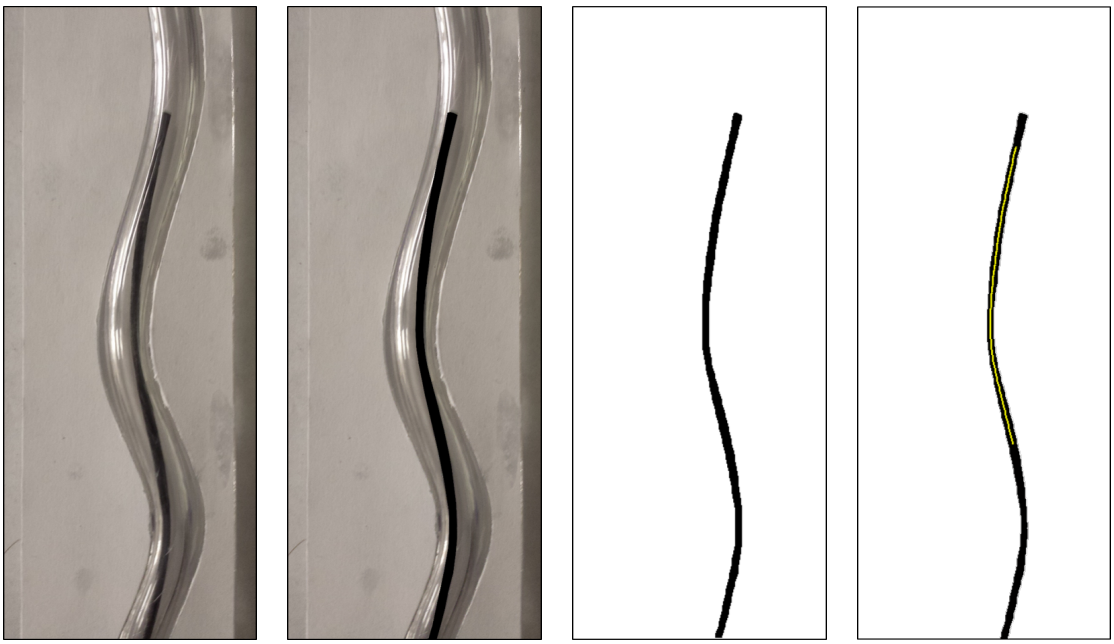

(a) (b) (c) (d)

Figure 5.3: General workflow for segmenation and generation of catheter shape midline for a single catheter pose. (a) Original image (b, c) Threshold segmentation (d) Segmened catheter with midpoint skeleton over tracked region of catheter.

	Linear	Piece-wise Shape Preserving	Hermite Cubic	Cubic Spline
Segment 1	0.407	0.404	0.407	0.405
Segment 2	0.407	0.195	0.380	0.240
Segment 3	0.481	0.484	0.484	0.521
Segment 4	0.531	1.103	0.533	1.015
Average	0.457	0.546	0.451	0.545

Table 5.1: Hausdorff distance for each interpolation algorithm in mm for each segment of the tracked shape catheter

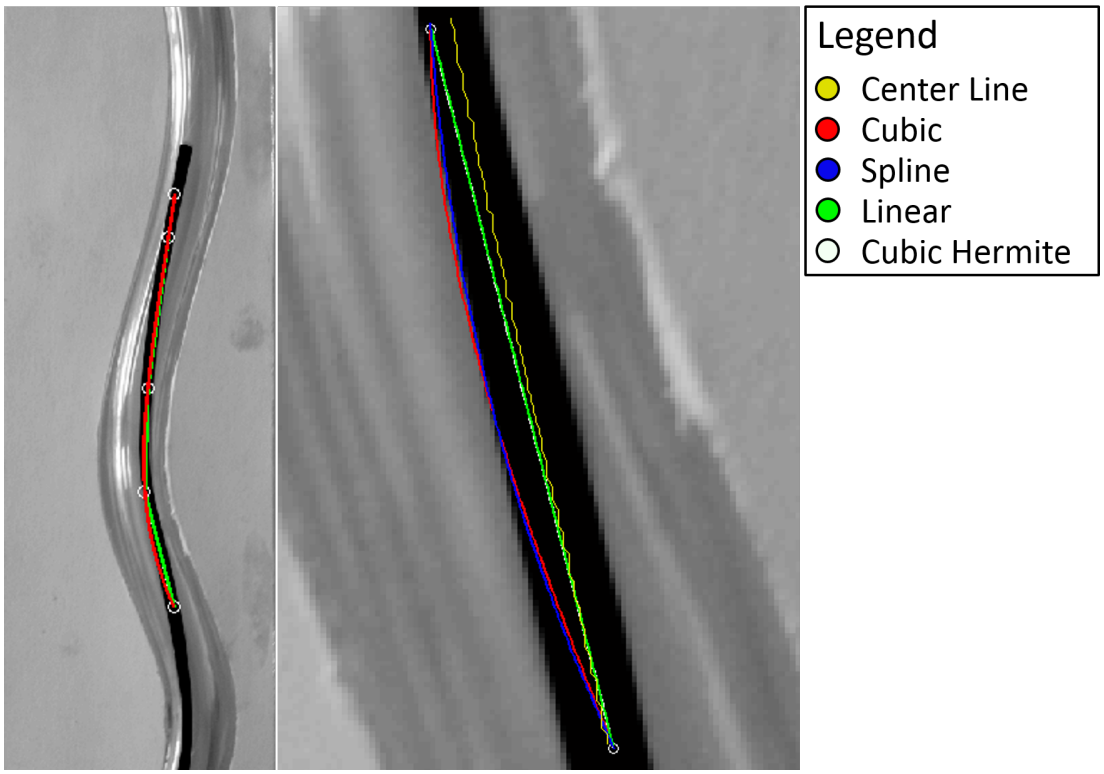

Figure 5.4: Full shape estimation with zoom on segment 4 of the catheter. Zoom image provided to demonstrate over estimation of shape for shape preserving and cubic spline.

5.5 Discussion and Conclusions

Image-guided surgery techniques applied to minimally invasive interventional vascular procedures has been shown to reduce exposure to ionizing radiation for both

	Linear	Piece-wise Shape Preserving Cubic	Hermite Cubic	Cubic Spline
Segment 1	0.0404	0.0414	0.0092	0.0414
Segment 2	0.0320	0.0453	0.0930	0.0377
Segment 3	0.2193	0.2209	0.1107	0.2420
Segment 4	0.2449	0.3619	0.0730	0.3505

Table 5.2: Average directional error values in millimeters for a single frame of the 2D centroid grid fluoroscope volume capture in millimeters. Error for the image intensifier fluoroscope is significantly higher than the solid state fluoroscope.

the patient and clinician. Ultimatley this results in lower absorbed dose lessening the risk of developing cancer atributted to the vascular procedure. Interventional cardiology accounts for the largest use of ionizing radiatoin among medical professions and the procedures performed each year is growing. While these vascular procedures save lives their inherent risk is considered minimal compared to the alternative of open heart surgery. IGS offers a solution that would allow for continued use of the current medical workflow for interventional cardiology while minimizing the risk of exposure.

Our previous work explored the application of IGS techniques to repair of atrial septal defects (ASD), a hole in the septum of the atria, which in in vitro studies resulted in a decreased radiation exposure level while still allowing the clinician to complete the procedure. While this work set the stage for application of IGS technqiues to vascular procedures a crucial missing feature was full representation of the catheter during image guidance. Lack of catheter shape information resulted in longer mock procedure times which in the case of IGS procedures resulted in no extra radiation dosage but would pose an issue when clinically translated due to increased procedure difficulty.

Application of spline interpolation algorithms to estimation of catheter shape allows the clinician to regain knowledge of catheter shape and orientation during

image guidance. Image guided procedures must be robust to noise and must handle any error in the system in a manner that results in the least impact on the patient. For this reason when evaluating interpolation algorithms we needed to not only determine how well the estimated shape matched the true shape but we also needed to ensure that the algorithm would underestimate shape in scenarios where there would be error. Our choice of using the Hausdorff distance as a metric for spline correlation stems from it providing the maximum of the collection of minimum distances between each point in both splines providing a maximum radius from which we can expect any point on the second subset to be away from the first subset. While the Hausdorff distance provides a means of comparing the actual and estimated splines it does not give an indication of how conservative the spline is in determining shape. Use of segment length error reveals the level of overestimation along the curve which in a clinical setting can result in display of incorrect locations.

Among the interpolation algorithms trialed during the experiments, we found that the tangents used at the provided control points play a large role in overall shape estimation particularly when there is a high degree of bending in the catheter segment. Tangent values based on the orientation of the tracker seeds are used in the hermite cubic spline interpolation allowing for a more constrained spline generation preventing shape overestimation. This constrained curve can be visualized in Figure 5.4 where the piece-wise shape preserving and cubic spline interpolation overestimated the extent of curvature in the shape in one segment of the catheter. Calculated Hausdorff distances in Table 5.1 grid provide a quantitative value of this overestimation which corresponds to what is seen visually. Segment length error (Table 5.2) for each catheter segment also revealed that cubic hermite splines were most conservative in their estimation closely resembling what would be attained using linear interpolation alone. Based on our results we believe that cubic hermite splines with tangents

based on the orientation of the tracking seeds will elicit the most conservative and accurate spline. Our future work will involve testing each algorithm in mock clinical trials to evaulate which algorithm provides the most clincial assitance to the catheter operator.

Chapter 6

Image-Guided Vascular Procedures: a feasability study

6.1 Introduction

Each year nearly 40,000 infants will be born with a congenital heart defect in the United States [59]. Congenital heart defects (CHD) are the most prevalent birth defect with recent trends signifying a growing rate in incidence [51]. From 1999 to 2006, 41,494 deaths in the United States were CHD related where 48% of these deaths occurred within the first year of life [30]. Treatment of CHDs depends on defect severity and can involve open heart surgery to repair structures in severe cases. In milder cases a cardiac catheterization procedure is used to deploy a device at a specific location to provide therapy through occlusion or patency support. We chose to target atrial septal defects in this study as means of determining the feasibility of using image-guidance to supplement the current procedure.

An atrial septal defect (ASD) is a congenital heart defect characterized by a left to right shunt between the atria resulting in irregular movement of blood. At birth

the interatrial shunt present during gestation normally closes allowing for movement of blood to the infant lungs. ASDs have a varied etiology and are classified based on anatomical location on the atrial septum. The three most prevalent types of ASDs are ostium secundum, ostium primum, and sinus venosus. Ostium secundum defects are centrally located and commonly form from the failed closing of the foramen ovale following birth. A patent foramen ovale in the case of an ostium secundum defect, is caused by the abnormal resorption of the septum primum causing incomplete adhesion to the septum secundum. This ultimately results in the formation of hole in the center of the septal wall that allows the exchange of oxygenated and deoxygenated blood in the heart. Symptoms include pale skin color, rapid breathing and shortness of breath. In less serious cases, children become easily tired during normal exercise and also present swelling in the extremities due to an inefficiently functioning cardiovascular system.

Ostium secundum defects can typically be repaired depending upon size through a cardiac catheterization procedure to deploy a device at a specific location to provide therapy through occlusion or patency support similar to Kings procedures. The progression of the delivery, deployment and release of a septal occluder in a patient can be seen in figure 1.3. The occluder typically used in procedures and seen in the provided images is the AMPLATZER Septal Occluder (St. Jude Medical). Design of this occluder includes two variably sized discs constructed from a Nitinol wire mesh with polyester embedded for tissue ingrowth. In between the occluder discs is a narrowing forming a waist that must match the defect diameter in size. Occluder delivery is a simple medical procedure compared to open heart surgery and offers comparable closure rates following placement with lower complication rates [20].

Cardiac catheterizations rely on fluoroscopic and ultrasound imaging to provide localization of the catheter during procedures. While ultrasound imaging is used

during procedures it is considered secondary to images provided by fluoroscopy that exposes patients to ionizing radiation. A 2008 study found that the heavy reliance on fluoroscopy in interventional cardiology resulted in 48% of the total ionizing radiation received by 50 consecutive patients admitted to a cardiology ward in Spain [10]. This high usage of radiation in interventional procedures poses a threat to patients with CHDs as they will require multiple procedures including follow-up examinations throughout their lives.

Investigation of radiation exposure to cardiac catheterization patients has been an active area of research for the past 15 years with many concluding there is a considerable cancer risk increase [8, 11, 44, 46, 52]. More importantly however is that children who undergo cardiac catheterizations are placed at even higher risk due to increased radiosensitivity. While methods have been developed to lessen exposure levels there is still heavy usage of fluoroscopy in pediatric cardiac catheterization labs [22, 62, 5, 6]. As incidence of CHD rises there is now an apparent need for the development of a solution that minimizes radiation exposure without significantly disrupting the current clinical workflow.

We propose the use of computer guided therapy techniques in cardiac catheterization procedures to reduce patient radiation exposure. In this work we demonstrate the feasibility of a paradigm shift away from ionizing radiation toward the use of electromagnetic (EM) catheter tracking for guidance of heart catheterizations using a mock atrial septal defect repair procedure.

6.2 Methods

6.2.1 Phantom Design

To validate EM guidance as a viable replacement for fluoroscopy a cardiac phantom was designed and 3D printed. The phantom consists of three parts representing a simplified anatomy of a heart with a defect on the septal wall (Figure 6.1a). Design of the phantom allows for easy changing of the septal wall and simplified retrieval of a deployed occluder. Multiple septal walls were designed to increase the difficulty of mock procedures as well as evaluate EM guidance in varying anatomical scenarios. The septum used in the mock procedures in this study, contains a 15 mm defect located centrally at the center and a close view can be seen in figure 6.1b.

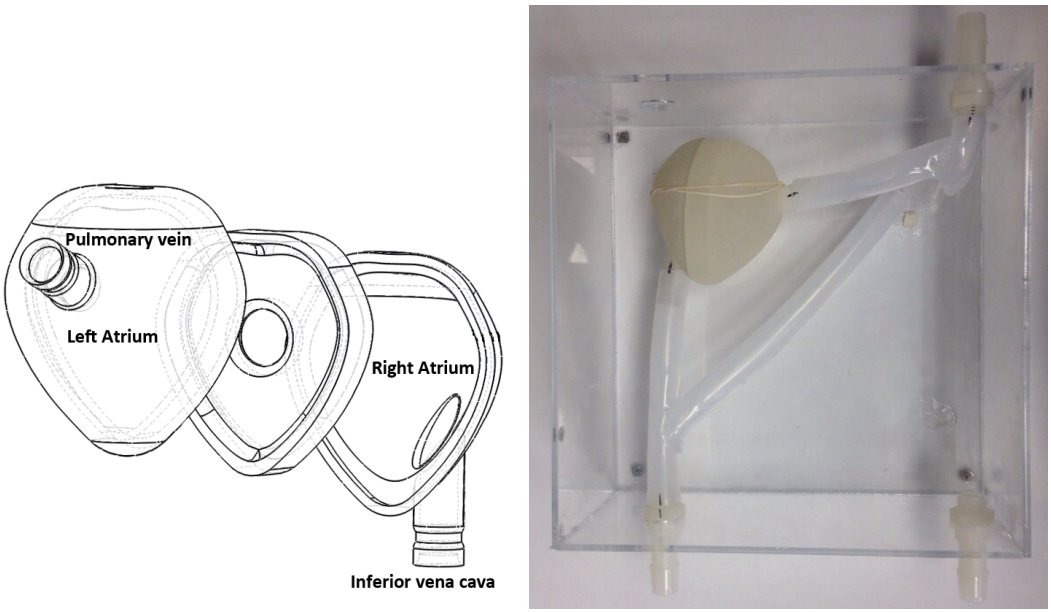

(a) (b)

Figure 6.1: (a) CAD design of cardiac phantom showing the separable parts. (b) Chest phantom with embedded cardiac phantom connected with polyethylene tubing to provide catheter access.

A chest phantom was constructed to allow for catheter access to the cardiac

phantom during mock procedures. The chest phantom is a 3 mm thick box 200 mm x 200 mm x 80 mm in size containing tubing simulating vasculature (Figure 6.1b. Fiducials were placed along the edges of the phantom at different locations to allow visualization in the desired plane as well prevent incorrect registrations due to the symmetry of the phantom. Each part of the chest phantom box was cut based on a CAD template using a laser-milling machine. Ports on the side of the chest phantom allow for catheter entry to the cardiac phantom positioned within the chest phantom. Tubing simulating vasculature was used to increase the difficulty in guidance of the catheter as well provide a more realistic test scenario.

6.2.2 EM Guidance

To accomplish EM guided repair of atrial septal defects we constructed several tracked tools. A 7 Fr catheter with five 5 degree-of-freedom (DOF) magnetic seeds embedded along the distal part of its inner lumen was designed and constructed first. Location for tracking seed placement along the lumen was determined by typical catheter visibility extent during procedures. The two seeds located at the distal end are placed closer to provide greater accuracy in spline calculations. Since the tracked catheter will be used to provide location of a sheath catheter the tip location must be represented accurately as tools will be deployed using its determined shape. An occluder delivery wire was tracked by placing a single 5DOF magnetic seed attached to its tip near the occluder attachment post.

Guidance of catheters was accomplished using Kit for Navigation by Image-Focused Exploration (KNIFE) as an image-guided surgery (IGS) platform paired with an Aurora (Northern Digital Instruments, Waterloo, ON, Canada) electromagnetic tracker. Fiducials placed on the chest phantom were used in a projective rigid body

registration algorithm to map the locations of tracked tools onto fluoroscopic images. The registration algorithm used requires the intrinsic parameters of the fluoroscope to allow for projective compensation. A KNIFE plugin was written to calculate a cubic hermite spline with tangents based on tracker seed orientations using reported tools locations. After calculation, the spline was rendered onto the precaptured bi-plane fluoroscopic images during EM guidance. In addition to the spline representing the constructed shape tool, the tip position and orientation of the guidewire currently in use was rendered.

During EM guided procedures, the location and orientation of the catheter and guidewire were updated in both planes in real time. This allowed the clinician the assess movements in both planes using synchronized data. Fluoroscopy guidance provided an updated image in a single plane while displaying the previous location in the other plane on a separate screen. This method requires asynchronous updating of position focusing on a single plane at a time. In addition, each fluoroscopic image update requires radiation where EM guidance facilitated by KNIFE will only need radiation for the reference images used.

6.2.3 Mock Procedures

An expert clinician guided a 10 Fr sheath catheter into position across the septal defect of a phantom heart where an occluder was then deployed. Since the occluder cannot be tracked using EM guidance, the occluder deployment segment of the procedure was done using fluoroscopy for both guidance methods. The occluder used in the study was an Amplatzer Septal Occluder constructed from a Nitinol mesh and polyester fibers that could be captured and deployed multiple times without damage. In order to seamlessly transition cardiac catheterizations to electromagnetic

guided procedures, fluoroscopic images remained the source of anatomical images for overlaying tool locations. A Toshiba bi-plane solid-state fluoroscope (Toshiba Inc., tawara-shi, Tochigi-ken, Japan) was used throughout the study for traditional guidance and capture of images used in EM guidance.

Figure 6.2: Mock clinical procedure setup with all equipment installed and prepared for running trials.

The EM guided mock procedure differed slightly from the fluoroscopy only guided procedure in a few steps. In order to track the sheath catheter the constructed shape tool was inserted into the lumen and fed to the catheter tip. With the shape tool embedded, the sheath catheter is guided into position across the phantoms septum using KNIFE and a foot pedal is used to hold the sheath catheter position on the screen. Holding the sheath catheter in place, the clinician removes the shape tool and inserts the tracked occluder delivery wire with the occluder already attached. Using KNIFE, the delivery wire is guided towards the sheath tip until the clinician determines that the first portion of the occluder can be delivered. The clinician is able to determine this without directly seeing the occluder position because there

is prior knowledge of between the tracking seed and the distal end of the loaded occluder. Then as for both guidance techniques, the occluder is deployed from the sheath catheter and its correct placement is achieved for each trial.

(a) KNIFE

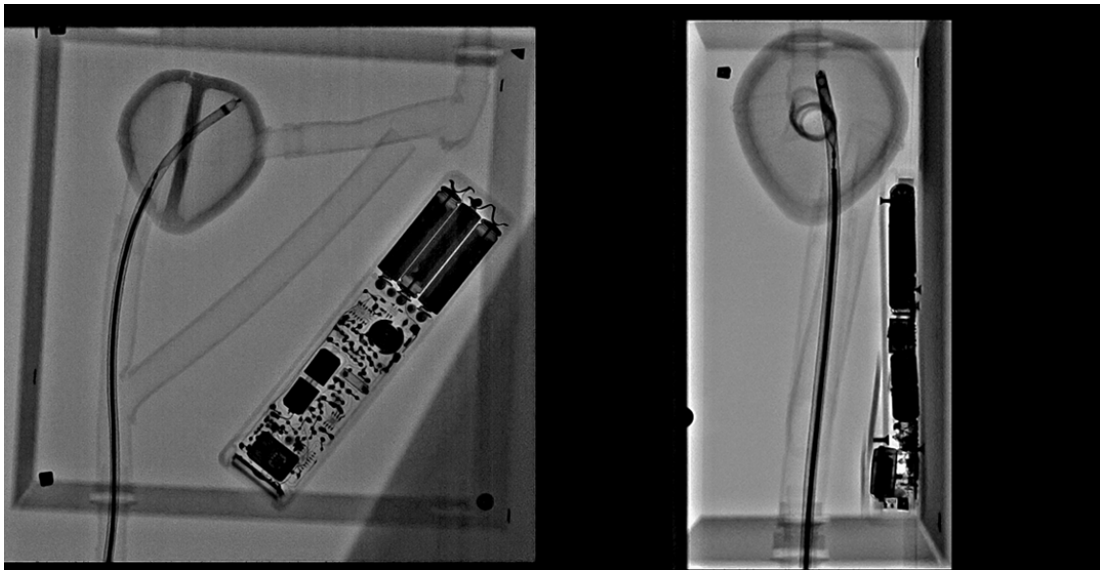

(b) Fluoroscopy

Figure 6.3: (a) KNIFE representation of catheter shape during mock procedures. (b) A fluoroscopy image of the catheter verfiying KNIFEs representaiton of catheter location and shape

For each procedure, the time taken to traverse to the defect was recorded as well as whether the occluder was successfully deployed. Radiation exposure experienced by the phantom was recorded for both guidance techniques using a Bleeper mR (Fluke Biomedical, Everett, WA) personal dosimeter. Measurement of effective dose as well as overall procedure time will quantify and provide a correlation between dose savings and procedure time. A two mean t-test was conducted to compare the procedure times and effective dose from each guidance technique.

6.3 Results

Each guidance method was run using the designed phantom for a total of 20 trials each with total time and radiation dose recorded. Using the image-guided surgery system KNIFE there was an average of 1.26 mSv of radiation dose with a range of 0.9 – 1.8 mSv. Traditional guidance required 3.33 mSv of radiation per procedure on average with a range of 2.21 – 4.9 mSv. A student t-test of the trials showed that KNIFE used a significantly lower amount of radiation than fluoroscopy guidance alone ($p < 0.01$) confirming that KNIFE reduces radiation use during mock procedures. The large variability in dose during fluoroscopy only procedures can easily be seen in the scatter plot of the trials and is quantified by the standard deviation which was nearly 0.9 mSv. KNIFE studies had less variation in the dose and due to this is reasonable to assume that the deployment aspect of the procedure requires around 1.26 mSv of dose. Using the fluoroscopy only dose as a full experiment dose, it can be inferred that KNIFE eliminates an average of 2.07 mSv of radiation dose to the patient.

Trials showed that the additional steps in the KNIFE guided procedure increased overall completion times. KNIFE trials took an average of 67 seconds with

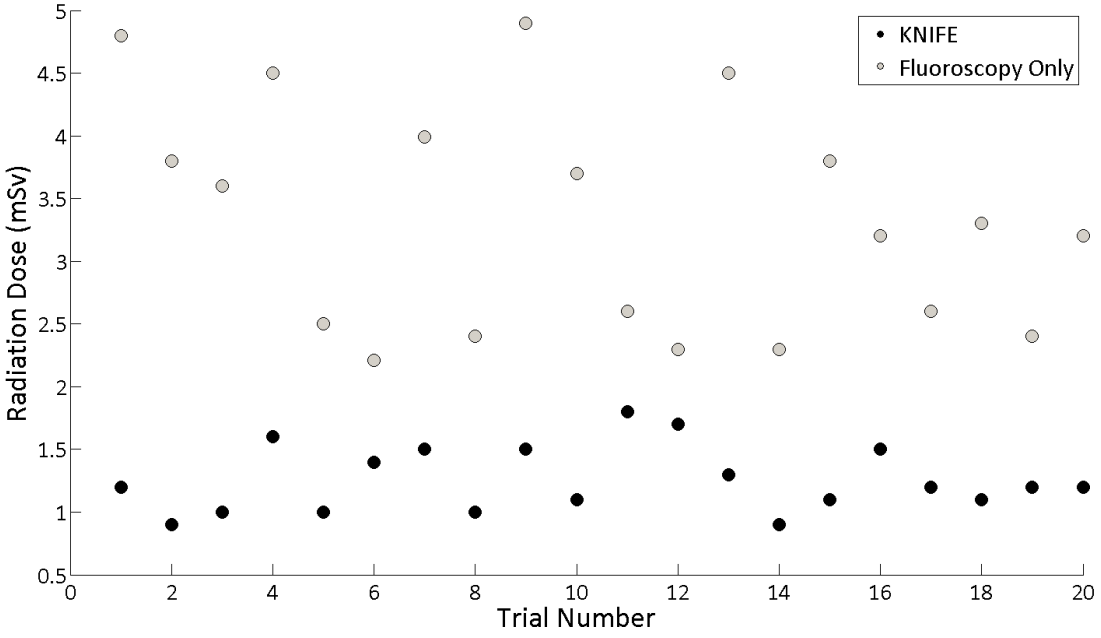

(a)

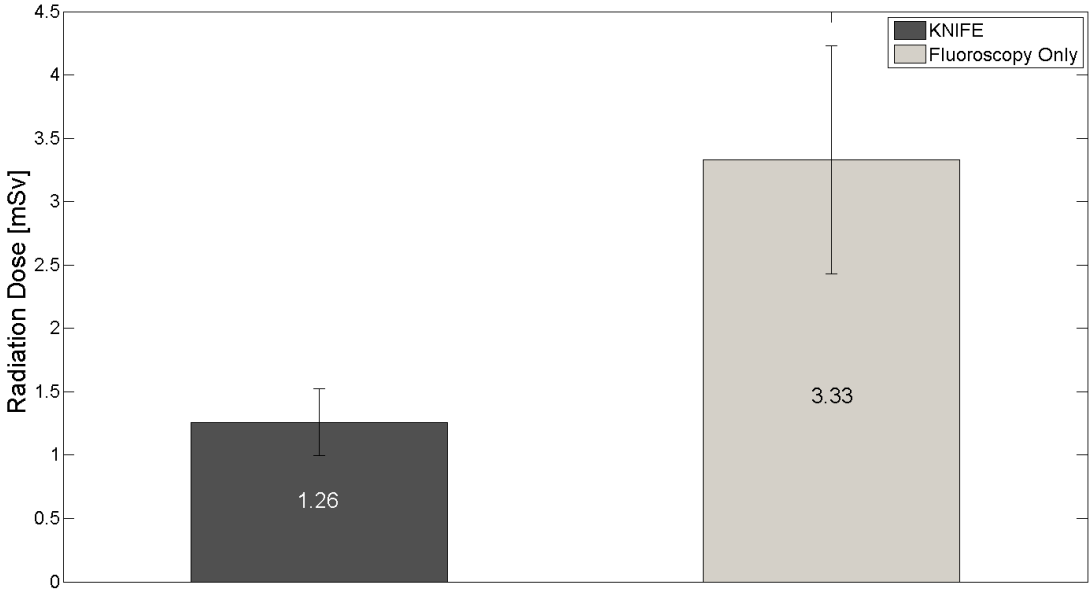

(b)

Figure 6.4: (a) Scatter plot of radiation dose for each mock trial. It is apparent there is a high degree of variability in fluoroscopy only guided procedures and the minimum radiation used was still higher than the maximum KNIFE dose. (b) Average radiation dose comparison where it can be inferred that since it took on average of 1.26 mSv of radiation to deploy the occluder, KNIFE saves an average of 2.07 mSv for the mock trials.

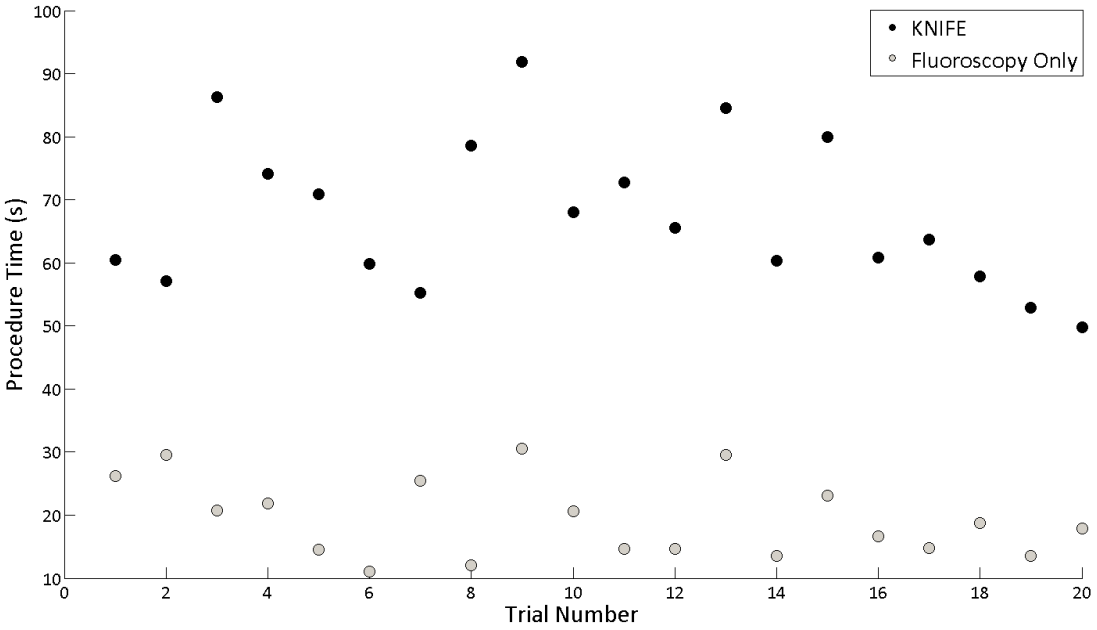

Figure 6.5: Scatter plot of the procedure times from the mock trials showing that KNIFE was significantly slower than fluoroscopy alone.

a range of 49.8 – 91.9 seconds. These times are significantly ($p < 0.01$) higher than the fluoroscopy only guided trials which had an average completion time of 19.49 seconds ranging from 11.1 – 30.6 seconds. Time for KNIFE guided trials had a large range due to trials where the catheter moved after placement or the software failed to recognize a requested position pause. Success of occluder deployment was recorded and each trial was successfully completed resulting in a 100% completion rate.

6.4 Discussion

Image-guided surgery techniques applied to cardiac catheterization procedures results in a reduction in radiation dose at the expense of procedure time. Since radiation dose is cumulative over lifetime a reduction in dose for even a segment of a procedure can lower the likelihood for the future development of cancer attributed to

the procedure. Over the past years the amount of interventional procedures performed has increased creating a greater need for even a partial solution to the radiation issue. While the negative implications of radiation exposure are highly outweighed by the necessity and benefit of the procedure IGS techniques offer a general solution without disrupting the current paradigm.

Concurrent measurement of radiation dose and procedure times allows for correlation between the variables identifying any trade-offs between the proposed image-guided procedure and the traditional approach. Average overall dose saving for KNIFE supplementation for our study was found to be nearly 62%, resulting in about 2.07 mSv dose savings. Timings for the trials showed that there was also a 246% increase in procedure time as a result of KNIFE use. It is apparent that in its current state, the developed system offers dose savings at the expense of time which for already lengthy procedures may not be suitable. Future versions of the system and procedure modifications will work towards closing the time gap between the two guidance techniques.

A second major tradeoff of reducing dose using an IGS system for guidance is the lack of real-time images. In this case, the phantom has no dynamic or moving parts but in the case of an animal or patient having real-time images would prevent the need for things like cardiac and respiratory motion compensation in image guidance systems. Procedure completion times may increase using IGS guidance depending on complexity and EM tracked tool design. In the mock procedures performed the requirement of pausing the sheath location, removing the shape catheter and inserting the delivery wire accounted for large portion of the procedure time. We believe that procedure time increases for image-guided procedures can be alleviated with the construction of more advanced EM tracked tools.

The results showed a large variation in the dose of the fluoroscopy only guided

procedures that can be attributed to small difficulties during the procedure such as traversing across the defect. Additionally, the dose varies because the clinician did not use fluoroscopy in the lateral plane for every procedure, using it only as needed. Since some mock procedures were easier to complete, the total dose experienced for a fluoroscopy only guided procedure is likely higher than what was recorded. While the recorded radiation dose values are not significant in terms of cancer risk they do however reveal there is room for improvement in ASD repair and other cardiac catheterization procedures. With a 100% completion rate for both guidance techniques, it shows that supplementation of fluoroscopy with IGS can lower radiation dose without preventing procedure success.

6.5 Conclusion

Through the methods developed we believe we have laid the groundwork for future inclusion of image-guidance techniques in fluoroscopy based catheter procedures. Our general approach is to study the procedure we plan to augment and find segments where image-guidance can supplement the current method. This method allows for a gradual shift of the current paradigm where even small changes in the procedure can yield desirable results like that shown in figure 6.4. The demonstrated approach is a novel solution for the reduction of radiation exposure in fluoroscopy guided vascular procedures. Future work will be concentrated towards evaluation in an animal model as well as expansion into repair of other CHDs such as aortic coarctation.

Chapter 7

Conclusions and Future Work

In this study I have reported on the application of image-guided surgery techniques to vascular interventional procedures. Results obtained have shown that a significant reduction in radiation dose is possible. Depending on future progress, it is expected that dose savings will increase further with the construction and subsequent use of novel tracked tools. As mentioned earlier, radiation dose is cumulative over lifetime and for pediatric patients the risk of cancer is higher due to increased sensitivity. Radiation dose reduction will be dependent upon procedure modification efforts using a combination of hardware and software approaches. A software approach would involve the use of projected points representing locations of untracked devices on the anatomical image overlay used by clinicians while a hardware approach would be focused around tool design.

While atrial septal defect was chosen by me as the specific disease of study, the methods developed are intended to be applicable to most if not all vascular procedures. Following the conclusion of this research, further work is expected to progress towards applying IGS to patients presenting with aortic coarctation (narrowing of the aorta). Currently, a coarctation phantom model has been constructed with pressure sensors

embedded within the lumen of tubing simulating vasculature. The phantom model will be used with an EM tracked balloon catheter to serve as validation for the effectiveness of IGS in coarctation repair. When the clinician guides the catheter into position and inflates the balloon, the sensors in the phantoms tubing will cause an LED to turn on, if pressure is applied. Design of phantoms with included procedure goals and success definitions is expected to reduce research effort and associated costs as animal model studies would make the breadth of this work prohibitively expensive.

Further work will include the addition of a representation of deployable devices without the use of an embedded tracking seed. Initial work in this domain is aimed at displaying the location of loaded septal occluders specifically AMPLATZER during mock procedures. The ideal goal would be to further reduce radiation dose exposure by allowing for devices to be deployed without the use of fluoroscopy. Using the extrinsic properties of the occluder the device tip will be displayed by projecting along the orientation vector of the distal tracking seed in the delivery wire. Overlay of device location will allow for deployment using KNIFE as previous work only displayed the tip of the delivery wire which was found to be inadequate during mock trials.

Novel tool design is expected to play a large role in this research as it progresses towards clinical translation since the current design uses the catheters lumen as a location for fixing tracking seeds. Using the current design, software must hold the shape and location of a sheath catheter that has already been guided into position with a custom built tracked shape tool. Ideally, the tracked seeds would be located within the wall of the catheter and could provide real-time update of shape without consuming the lumen, allowing for guide wire and tool delivery. Tracking seeds currently used have a 0.5 mm diameter making them suitable for placement in the catheter wall without the need for drastically increasing the outer diameter or

decreasing the inner diameter of the catheter. Construction of catheters with tracked seeds, embedded in the walls, permits live tracking of delivery sheaths and the tools guided through them.

A key aspect of future work will be determining what information should be presented to the clinician to not only create a medically relevant system but also to reduce the chance of complication during procedures. Initial iterations of the IGS system lacked features that were later deemed necessary to successfully completing procedures. Closer work with the research clinician will provide valuable insight into creating a streamlined procedure that could work in a clinical scenario. Since the extent of this work is wide reaching it is difficult to foresee every avenue of future study and the suggestions offered are not comprehensive. There is a real need for the technology developed in this work and the benefits it can provide, warrant further commitment to its underlying research goal.

Bibliography

[1] The 2007 recommendations of the international commission on radiological protection. icrp publication 103. *Ann ICRP*, 37(2-4):1–332, 2007.

[2] Cancer facts & figures 2013. Report, American Cancer Society, Inc., 2013.

[3] Emerson rose act, 2013.

[4] NEMA PS3 / ISO 12052. Digital imaging and communications in medicine (dicom) standard, 1985.

[5] E. Abdelaal, G. Plourde, J. Machaalany, J. Arsenault, G. Rimac, J. P. Dry, G. Barbeau, E. Larose, R. De Larochellire, C. M. Nguyen, R. Allende, H. Ribeiro, O. Costerousse, R. Mongrain, O. F. Bertrand, and Interventional Cardiologists at Quebec Heart-Lung Institute. Effectiveness of low rate fluoroscopy at reducing operator and patient radiation dose during transradial coronary angiography and interventions. *JACC Cardiovasc Interv*, 2014.

[6] A. A. Abu Hazeem, Y. Dori, K. K. Whitehead, M. A. Harris, M. A. Fogel, M. J. Gillespie, J. J. Rome, and A. C. Glatz. X-ray magnetic resonance fusion modality may reduce radiation exposure and contrast dose in diagnostic cardiac catheterization of congenital heart disease. *Catheter Cardiovasc Interv*, 2014.

[7] L. Ait-Ali, M. G. Andreassi, I. Foffa, I. Spadoni, E. Vano, and E. Picano. Cumulative patient effective dose and acute radiation-induced chromosomal dna damage in children with congenital heart disease. *Heart*, 96(4):269–74, 2010.

[8] M. G. Andreassi. Radiation risk from pediatric cardiac catheterization: friendly fire on children with congenital heart disease. *Circulation*, 120(19):1847–9, 2009.

[9] M. G. Andreassi, L. Ait-Ali, N. Botto, S. Manfredi, G. Mottola, and E. Picano. Cardiac catheterization and long-term chromosomal damage in children with congenital heart disease. *Eur Heart J*, 27(22):2703–8, 2006.

[10] G. Bedetti, N. Botto, M. G. Andreassi, C. Traino, E. Vano, and E. Picano. Cumulative patient effective dose in cardiology. *Br J Radiol*, 81(969):699–705, 2008.

[11] L. Beels, K. Bacher, D. De Wolf, J. Werbrouck, and H. Thierens. gamma-h2ax foci as a biomarker for patient x-ray exposure in pediatric cardiac catheterization: are we underestimating radiation risks? *Circulation*, 120(19):1903–9, 2009.

[12] Jerrold Bushberg and Anthony Seibert. *The Essential of Physics of Medical Imaging*. Lippincott Williams & Wilkens, Philadelphia, PA, 2002.

[13] ISEMIR Working Group on Interventional Cardiology. Report on the questionnaires on occupational exposure in interventional cardiology. Report, 2010.

[14] Dev P. Chakraborty. Image intensifier distortion correction. *Medical Physics*, 14(2):249–252, 1987.

[15] Paul S Cho and Roger H Johnson. Automated detection of bb pixel clusters in digital fluoroscopic images. *Physics in Medicine and Biology*, 43(9), 1998.

[16] Foster Corporation. Radiopaque compounds.

[17] C. Cousins, D. L. Miller, G. Bernardi, M. M. Rehani, P. Schofield, E. Vano, A. J. Einstein, B. Geiger, P. Heintz, R. Padovani, K. H. Sim, and Protection International Commission on Radiological. Icrp publication 120: Radiological protection in cardiology. *Ann ICRP*, 42(1):1–125, 2013.

[18] A. R. Cowen, A. G. Davies, and M. U. Sivananthan. The design and imaging characteristics of dynamic, solid-state, flat-panel x-ray image detectors for digital fluoroscopy and fluorography. *Clinical Radiology*, 63(10):1073–1085, 2008.

[19] Alessio Dore, Gabrijel Smoljkic, Emmanuel Poorten, Mauro Sette, Jos Sloten, and Guang-Zhong Yang. Catheter navigation based on probabilistic fusion of electromagnetic tracking and physically-based simulation, 2012.

[20] Zhong-Dong Du, Ziyad M. Hijazi, Charles S. Kleinman, Norman H. Silverman, Kinley Larntz, and Investigators Amplatzer. Comparison between transcatheter and surgical closure of secundum atrial septal defect in children and adults: Results of a multicenter nonrandomized trial. *Journal of the American College of Cardiology*, 39(11):1836–1844, 2002.

[21] A. Enquobahrie, P. Cheng, K. Gary, L. Ibanez, D. Gobbi, F. Lindseth, Z. Yaniv, S. Aylward, J. Jomier, and K. Cleary. The image-guided surgery toolkit igstk: An open source c++ software toolkit. *J Digit Imaging*, 20(Suppl 1):21–33, 2007.

[22] F. F. Faletra, G. Pedrazzini, E. Pasotti, S. Muzzarelli, M. C. Dequarti, R. Murzilli, S. A. Schlossbauer, I. P. Slater, and T. Moccetti. 3d tee during catheter-based interventions. *JACC Cardiovasc Imaging*, 7(3):292–308, 2014.

[23] Pascal Fallavollita. Is single-view fluoroscopy sufficient in guiding cardiac ablation procedures? *International Journal of Biomedical Imaging*, 2010, 2010.

[24] K. Faulkner and A. Werduch. An estimate of the collective dose to the european population from cardiac x-ray procedures. *Br J Radiol*, 81(972):955–62, 2008.

[25] FDA. White paper: Initiative to reduce unnecessary radiation exposure from medical imaging. Report, 2011.

[26] T Feldman. Interventional cardiology manpower needs: How many of us are there? how many should there be? how many will we need in the future? catheterization and cardiovascular interventions, 2003.

[27] R. L. Galloway and R. J. Maciunas. Stereotactic neurosurgery. *Crit Rev Biomed Eng*, 18(3):181–205, 1990.

[28] K. Gary, L. Ibanez, S. Aylward, D. Gobbi, M. B. Blake, and K. Cleary. Igstk: an open source software toolkit for image-guided surgery. *Computer*, 39(4):46–53, 2006.

[29] D. Gering, A. Nabavi, R. Kikinis, W. Grimson, N. Hata, P. Everett, F. Jolesz, and Iii W. Wells. An integrated visualization system for surgical planning and guidance using image fusion and interventional imaging. *Int Conf Med Image Comput Comput Assist Interv.*, 2:809–819., 1999.

[30] S. M. Gilboa, J. L. Salemi, W. N. Nembhard, D. E. Fixler, and A. Correa. Mortality resulting from congenital heart disease among children and adults in the united states, 1999 to 2006. *Circulation*, 122(22):2254–63, 2010.

[31] J. I. Hoffman and S. Kaplan. The incidence of congenital heart disease. *Journal of the American College of Cardiology*, 39(12):1890–1900, 2002.

[32] A. K. Jain, T. Mustafa, Y. Zhou, C. Burdette, G. S. Chirikjian, and G. Fichtinger. Ftrac–a robust fluoroscope tracking fiducial. *Med Phys*, 32(10):3185–98, 2005.

[33] R. L. Jensen, J. L. Stone, and R. A. Hayne. Introduction of the human horsley-clarke stereotactic frame. *Neurosurgery*, 38(3):563–7; discussion 567, 1996.

[34] D. R. Johnson, J. Kyriou, E. J. Morton, A. Clifton, M. Fitzgerald, and E. Macsweeney. Radiation protection in interventional radiology. *Clin Radiol*, 56(2):99–106, 2001.

[35] T. D. King, S. L. Thompson, C. Steiner, and N. L. Mills. Secundum atrial septal defect. nonoperative closure during cardiac catheterization. *JAMA*, 235(23):2506–9, 1976.

[36] M. K Konings, E. B. van de Kraats, T. Alderliesten, and W. J. Niessen. Analytical guide wire motion algorithm for simulation of endovascular interventions., 2003.

[37] Y. Kosugi, E. Watanabe, J. Goto, T. Watanabe, S. Yoshimoto, K. Takakura, and J. Ikebe. An articulated neurosurgical navigation system using mri and ct images. *IEEE Trans Biomed Eng.*, 35(2):147–52., 1988.

[38] David Kwartowitz, Fuad Mefleh, and George Baker. Towards image-guided atrial septal defect repair: an ex vivo analysis. In *SPIE: Medical Imaging*.

[39] F. Manstad-Hulaas, G. A. Tangen, T. Dahl, T. A. Hernes, and P. Aadahl. Three-dimensional electromagnetic navigation vs. fluoroscopy for endovascular aneurysm repair: a prospective feasibility study in patients. *J Endovasc Ther*, 19(1):70–8, 2012.

[40] C. J. Martin. A review of radiology staff doses and dose monitoring requirements. *Radiat Prot Dosimetry*, 136(3):140–57, 2009.

[41] D. A. Mauriello, K. A. Fetterly, R. J. Lennon, G. S. Reeder, N. W. Taggart, D. J. Hagler, F. Cetta, and A. K. Cabalka. Radiation reduction in pediatric and adult congenital patients during cardiac catheterization. *Catheter Cardiovasc Interv*, 2014.

[42] P. D. McGrath, D. E. Wennberg, J. D. Dickens, A. E. Siewers, F. L. Lucas, D. J. Malenka, M. A. Kellett, and T. J. Ryan. Relation between operator and hospital volume and outcomes following percutaneous coronary interventions in the era of the coronary stent. *JAMA*, 284(24):3139–44, 2000.

[43] Fuad Mefleh, Hamilton Baker, and David Kwartowitz. Efficacy of a novel igs system in atrial septal defect repair, 2013.

[44] B. Modan, L. Keinan, T. Blumstein, and S. Sadetzki. Cancer following cardiac catheterization in childhood. *Int J Epidemiol*, 29(3):424–8, 2000.

[45] Kiyokazu Nakajima, Jeffrey W. Milsom, and Bartholomus Bhm. History of laparoscopic surgery. pages 1–9, 2006.

[46] M. K. Natarajan, N. Paul, M. Mercuri, E. J. Waller, J. Leipsic, M. Traboulsi, H. S. Banijamali, L. Benson, T. N. Sheth, C. S. Simpson, A. Brydie, M. P. Love, R. Gallo, Secondary Panel:, and Canadian Cardiovascular Society. Canadian cardiovascular society position statement on radiation exposure from cardiac imaging and interventional procedures. *Can J Cardiol*, 29(11):1361–8, 2013.

[47] Mike O'Riordan. *Radiation protection : a memoir of the National Radiological Protection Board*. Health Protection Agency, Didcot, 2007.

[48] Nobuyuki Otsu. A threshold selection method from gray-level histograms. *Systems, Man and Cybernetics, IEEE Transactions on*, 9(1):62–66, 1979.

[49] R. Padovani. Assessing and reducing exposures to cardiology staff. In *Radiation Protection in Medicine: Radiation protection of patients and staff in interventional procedures*. International Atomic Energy Agency (IAEA).

[50] R. Padovani and C. A. Rodella. Staff dosimetry in interventional cardiology. *Radiat Prot Dosimetry*, 94(1-2):99–103, 2001.

[51] S. E. Parker, C. T. Mai, M. A. Canfield, R. Rickard, Y. Wang, R. E. Meyer, P. Anderson, C. A. Mason, J. S. Collins, R. S. Kirby, A. Correa, and National Birth Defects Prevention Network. Updated national birth prevalence estimates for selected birth defects in the united states, 2004-2006. *Birth Defects Res A Clin Mol Teratol*, 88(12):1008–16, 2010.

[52] K. Perisinakis, J. Damilakis, N. Theocharopoulos, E. Manios, P. Vardas, and N. Gourtsoyiannis. Accurate assessment of patient effective radiation dose and associated detriment risk from radiofrequency catheter ablation procedures. *Circulation*, 104(1):58–62, 2001.

[53] Charles Petzold. *Programming Windows (Developer Reference)*. Microsoft Press, Redmond, WA, 5 edition, 1999.

[54] International Commission on Radiation Protection. Radiation and your patient: a guide for medical practitioners, 2012.

[55] Committee to Assess Health Risks from Exposure to Low Levels of Ionizing Radiation. Health risks from exposure to low levels of ionizing radiation: Beir vii phase 2. Report, 2006.

[56] United Nations Scientific Committee on the Effects of Atomic Radiation. Source and effects of ionizing radiation, 2008.

[57] Lav Rai, Jason Gibbs, and Henky Wibowo. A c-arm calibration method with application to fluoroscopic image-guided procedures. pages 831625–831625, 2012.

[58] D. A. Reimann and M. J. Flynn. Automated distortion correction of x-ray image intensifier images. In *Nuclear Science Symposium and Medical Imaging Conference, 1992., Conference Record of the 1992 IEEE*, pages 1339–1341 vol.2.

[59] M. D. Reller, M. J. Strickland, T. Riehle-Colarusso, W. T. Mahle, and A. Correa. Prevalence of congenital heart defects in metropolitan atlanta, 1998-2005. *J Pediatr*, 153(6):807–13, 2008.

[60] M. E. Rettmann, 3rd Holmes, D. R., B. M. Cameron, and R. A. Robb. An event-driven distributed processing architecture for image-guided cardiac ablation therapy. *Comput Methods Programs Biomed*, 95(2):95–104, 2009.

[61] Eisenberg Rl. *Radiology, an illustrated history.* Mosby Year Book, St. Louis, 1992.

[62] S. Schubert, S. Kainz, B. Peters, F. Berger, and P. Ewert. Interventional closure of atrial septal defects without fluoroscopy in adult and pediatric patients. *Clin Res Cardiol*, 2012.

[63] J. A. Seibert. Flat-panel detectors: how much better are they? *Pediatr Radiol*, 36 Suppl 2:173–81, 2006.

[64] Delia Soimu, Cristian Badea, and Nicolas Pallikarakis. A novel approach for distortion correction for x-ray image intensifiers. *Computerized Medical Imaging and Graphics*, 27(1):79 – 85, 2003.

[65] J. D. Stefansic, W. A. Bass, S. L. Hartmann, R. A. Beasley, T. K. Sinha, D. M. Cash, A. J. Herline, and Jr. Galloway, R. L. Design and implementation of a pc-based image-guided surgical system. *Comput Methods Programs Biomed*, 69(3):211–24, 2002.

[66] N. Suhm, P. Mueller, M. Hehli, S. Koller, U. Bopp, A. L. Jacob, P. Regazzoni, and P. Messmer. Adapting the fluoroscope to image-guided surgery. *Injury*, 34(4):307–11, 2003.

[67] OFFIS Institute for Information Technology. Dicom toolkit (dcmtk), 1995 - Present.

[68] E. Vano, L. Gonzalez, J. M. Fernandez, F. Alfonso, and C. Macaya. Occupational radiation doses in interventional cardiology: a 15-year follow-up. *Br J Radiol*, 79(941):383–8, 2006.

[69] L. Venneri, F. Rossi, N. Botto, M. G. Andreassi, N. Salcone, A. Emad, M. Lazzeri, C. Gori, E. Vano, and E. Picano. Cancer risk from professional exposure in staff working in cardiac catheterization laboratory: insights from the national research council's biological effects of ionizing radiation vii report. *Am Heart J*, 157(1):118–24, 2009.

[70] A. W. Wassef, B. Hiebert, A. Ravandi, J. Ducas, K. Minhas, M. Vo, M. Kass, G. Parmar, and F. Hussain. Radiation dose reduction in the cardiac catheterization laboratory utilizing a novel protocol. *JACC Cardiovasc Interv*, 2014.

[71] L. Weise, S. Eibach, V. Seifert, and M. Setzer. Intraoperative 3d fluoroscopy in stereotactic surgery. *Acta Neurochir (Wien)*, 154(5):815–21, 2012.

[72] Jay B. West, Rasool Khadem, and Jr Calvin R. Maurer. Overcoming the distortion problem in image-enhanced fluoroscopy. pages 344–353, 2003.

[73] Jay B. West and Jr Calvin R. Maurer. A system for finding a 3d target without a 3d image. pages 69180J–69180J, 2008.

[74] Gang Xu and Zhengyou Zhang. *Epipolar Geometry in Stereo, Motion and Object Recognition*, volume 6. Springer, 1996.

[75] E. N. Yakoumakis, G. I. Gialousis, D. Papadopoulou, T. Makri, Z. Pappouli, N. Yakoumakis, P. Papagiannis, and E. Georgiou. Estimation of children's radiation dose from cardiac catheterisations, performed for the diagnosis or the treatment of a congenital heart disease using tld dosimetry and monte carlo simulation. *J Radiol Prot*, 29(2):251–61, 2009.

[76] L. Yatziv, M. Chartouni, S. Datta, and G. Sapiro. Toward multiple catheters detection in fluoroscopic image guided interventions. *IEEE Trans Inf Technol Biomed*, 16(4):770–81, 2012.

[77] W.Q. Zhang, K.R. Dai, and C.T. Wang. Novel method for correction of x-ray fluoroscopic image. In *Engineering in Medicine and Biology*, pages 6340 – 6343.